

Exocomet models in transit: light curve morphology in the optical – near infrared wavelength range

SZILÁRD KÁLMÁN,^{1,2,3,4} GYULA M. SZABÓ,^{3,5} AND CSABA KISS^{1,2,6}

¹*Konkoly Observatory, HUN-REN Research Centre for Astronomy and Earth Sciences, Konkoly Thege 15-17, 1121 Budapest, Hungary*

²*HUN-REN CSFK, MTA Centre of Excellence, Budapest, Hungary*

³*HUN-REN-ELTE Exoplanet Research Group, Szombathely, Szent Imre h. u. 112., H-9700, Hungary*

⁴*ELTE Eötvös Loránd University, Doctoral School of Physics, Budapest, Pázmány Péter sétány 1/A, H-1117, Hungary*

⁵*ELTE Eötvös Loránd University, Gothard Astrophysical Observatory, Szombathely, Szent Imre h. u. 112., H-9700, Hungary*

⁶*Institute of Physics and Astronomy, ELTE Eötvös Loránd University, Budapest, Hungary*

ABSTRACT

Following the widespread practice of exoplanetary transit simulations, various presumed components of an extrasolar system can be examined in numerically simulated transits, including exomoons, rings around planets, and the deformation of exoplanets. Template signals can then be used to efficiently search for light curve features that mark specific phenomena in the data, and they also provide a basis for feasibility studies of instruments and search programs. In this paper, we present a method for exocomet transit light curve calculations using arbitrary dust distributions in transit. The calculations, spanning four distinct materials (carbon, graphite, pyroxene, and olivine), dust grain sizes (100 nm – 300 nm, 300 nm – 1000 nm, and 1000 nm – 3000 nm) encompass light curves in VRJHKL bands. We also investigated the behavior of scattering colors. We show that multicolor photometric observations are highly effective tools in the detection and characterization of exocomet transits. They provide information on the dust distribution of the comet (encoded in the light curve shape), while the color information itself can reveal the particle size change and material composition of the transiting material, in relation to the surrounding environment. We also show that the typical cometary tail can result in the wavelength dependence of the transit timing. We demonstrate that multi-wavelength observations can yield compelling evidence for the presence of exocomets in real observations.

Keywords: Exocomets(2368) — Comet tails(274) — Multi-color photometry(1077) — Radiative transfer simulations(1967)

1. INTRODUCTION

Comets, mostly known as spectacular sojourners on our skies (Kronk et al. 2017), have been counted for a long time among the most ancient reservoirs of solid material and ice in the Solar System. As witnesses of the formation of the outer Solar System (e.g. Donn 1963; Encrenaz 1984; Vidmachenko & Steklov 2013), their orbits can evolve through gravitational perturbations, causing them to migrate to the inner Solar System – in a process that presumably happens very similarly in the extrasolar systems as well (e.g. Graham et al. 2007; Matrà et al. 2017). Comets are believed to be one of the possible sources of water and nitrogen (e.g. Marty 2012; Altwegg et al. 2015; Poch et al. 2020) and possibly even organic material on Earth (e.g. Fray et al. 2016; d’Ischia et al. 2021). They are therefore invoked as essentials for the volatiles and habitability of Earth and, based on this analogy, also on other planetary systems (e.g. Kral et al. 2018). Thus, these objects are also important from an astrobiological perspective (Welsh 2019).

Compared to the ~ 4150 known exoplanetary systems at the time of writing, there are only a few systems in which exocometary activity has been detected. There are two main approaches to the detection of extrasolar comets: photometry and spectroscopy (Pavlenko et al. 2021). In the circumstellar disk of the β Pictoris system, Ferlet et al. (1987) detected time-variable features in Ca II H & K spectral lines, which are attributed to the so-called Falling

Evaporating Bodies (FEBs [Beust et al. 1994](#); [Lagrange-Henri et al. 1989](#); [Beust & Morbidelli 2000](#)). Given that FEBs were first detected and are perhaps the most studied in the β Pictoris system ([Beust & Valiron 2007](#); [Tobin et al. 2019](#)), these spectroscopic transients are also known as β Pic-like phenomena. [Kiefer et al. \(2014b\)](#) identified 493 individual exocomets in β Pictoris through the study of these features. The large number of comets detected allowed for a clustering of these objects, yielding two groups of distinct origins and properties ([Kiefer et al. 2014b](#); [Roberge 2014](#)). Observations of FEBs are not limited to the β Pic system. [Redfield \(2007\)](#) detected time-dependent absorption features in the Na I D doublet of HD 32297, which is related to the debris disk surrounding the star. Other well-known examples include HD 172555 ([Kiefer et al. 2014a](#); [Grady et al. 2018](#)), HD 100546 ([Grady et al. 1997](#)), HD 24966, HD 38056, HD 79469 and HD 225200 ([Welsh & Montgomery 2018](#)). As a further step in interpreting these spectroscopic observations, [Kennedy \(2018\)](#) proposed a method to retrieve some of the orbital elements of the exocomets in question. [Rebollido et al. \(2020\)](#) carried out a large spectroscopic survey of (suspected) exocomet host stars, finding that 17% of stars showing near infra-red excess allow for a detection of FEB-like events, suggesting a weak link between the evolution of a protoplanetary disk and the features attributed to exocomets.

The FEB-detections listed above rely on spectroscopic time series observations, which are complicated by nature. [Lecavelier Des Etangs et al. \(1999\)](#) proposed the characteristic “round triangle” shape of exocometary transits, which are thought to be photometric counterparts of the FEBS ([Zieba et al. 2019](#)), and subsequently constructed a library of various transit shapes ([Lecavelier Des Etangs 1999](#)). [Lecavelier Des Etangs et al. \(1999\)](#) present a light curve model constructed of two components: extinction and forward scattering, both of which are based on physical modeling of cometary activity. The total contribution of these effects depends strongly on the grain size of the dust (and gas) emitted from the comet as well as on its dust production rate. The shapes of the transit light curves that result are colloquially called “sharkfins”. These transit events are naturally detectable in long baseline datasets of survey-type space observatories, such as *Kepler* ([Borucki et al. 2010](#)), *TESS* ([Ricker et al. 2015](#), Transiting Exoplanet Survey Satellite) or the upcoming *PLATO* ([Rauer et al. 2014](#), PLANetary Transits and Oscillations of stars). *TESS* also revealed several hundred so-called dippers ([Tajiri et al. 2020](#)), which are generally young stars characterized by transients with variable depth and lasting characteristically for 0.5–1 days. These transients are thought to have multiple origins, from the disk warps and accretion columns of T tauri stars (represented by rather periodic signals) to the transit of giant exocomets in the line of sight (represented by aperiodic components). [Strøm et al. \(2020\)](#) also discussed the possibility of interstellar comets as the origin of the signals which would naturally be single-occurrence events. Although the low rate of periodicity in a system is a diagnostic of the presence of exocomets, there is still a need for independent evidence for the cometary origin ([Tajiri et al. 2020](#); [Gaidos et al. 2022](#); [Gaidos 2022](#)).

The detection of exocomet transits ([Rappaport et al. 2018](#); [Zieba et al. 2019](#); [Kennedy et al. 2019](#); [Lecavelier des Etangs et al. 2022](#); [Kiefer et al. 2023](#)) often relies on pattern search methods¹ (including the box-fitting approach of [Kennedy et al. 2019](#), that has to include a false-positive rejection step due to exoplanets, binary stars etc.), which are known to be sensitive only to patterns that were used for training. In case of the box-fitting approach, this sensitivity arises at the false-positive rejection step. Most “exocomet transit” photometric transients indeed represent a sharkfin-like feature, but these are the features the methods are looking for. With a sophisticatedly trained pattern generator, we can derive template light curves of transiting exocomets that we can include in the actual search and interpretation efforts.

In this paper, we utilize a simple model to generate synthetic exocometary transit light curves. We put comet-like model distributions into transit and calculate the radiation transfer as a function of the angle of the incident backlight. We present template light curves from these transit simulations from optical to near-infrared (NIR) wavelengths. We also explore the “color of comet dust” (e.g. [Kolokolova et al. 2001](#); [Levasseur-Regourd et al. 2007](#)) when transiting a star, comparing the effect of dust size and material dependence along the examined wavelengths.

The paper is structured as follows. In Sect. 2 we describe the exocomet models, as well as the light curve simulations (including both extinction and forward scattering). In Sect. 3, we present a library of light curves that are made publicly available. In Sect. 4, we place our models into context and consider the possible implications regarding the future of the hunt for exocomets.

2. METHODS

2.1. Radiative transfer modeling

¹ Private communication with S. Zieba

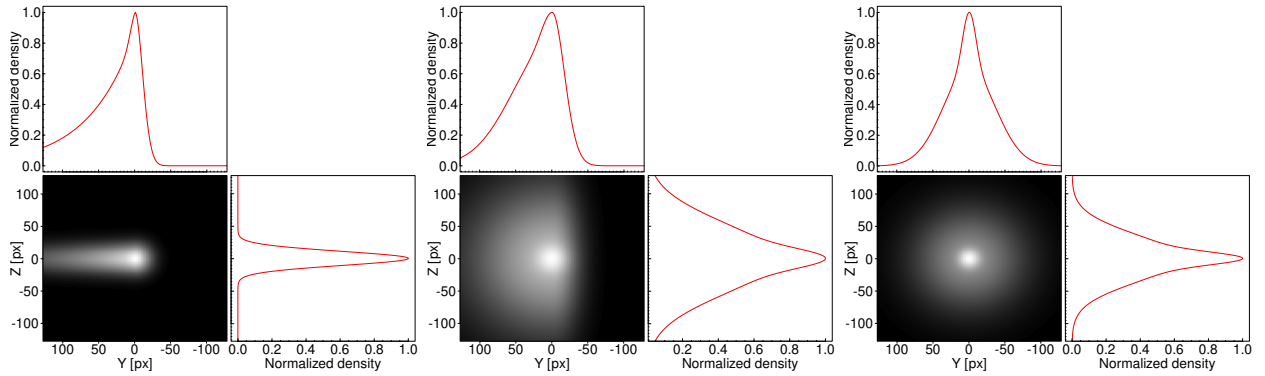


Figure 1. Density distribution of the comet models in this study. The figure panels show the comet with a narrow tail, the comet with a fan-like tail and the comet without a tail. The 2D images show the comet models as seen in reflected light in sky projection, together with the projected densities on the y and z axis (top and bottom right panels).

Radiative transfer modeling of dust structures, assumed to be responsible for the obscuration of stellar light in transient phenomena, is performed using RADMC-3D (Dullemond et al. 2012). RADMC-3D is a freely available open source code package for diagnostic radiative transfer calculations. It calculates, for a given geometrical distribution of gas and/or dust, what its images and/or spectra look like when viewed from a certain angle, including optical depth calculations, both in scattered light and in thermal emission. To perform exocomet light curve synthesis, we use RADMC-3D 2.0 and a volume of 256^3 cells in Cartesian coordinates, with a box edge size adjusted to the actual density distribution (see Sect. 2.3), typically in the order of 0.05 au. The center of the coordinate system is the center of the simulation volume. The central star is located at a distance of r_h from the center of the coordinate system on the x-axis, outside the simulation volume. We considered two cases: a ‘solar-like’ star (with a photospheric temperature of 5780 K a radius of $R_\odot = 6.96 \times 10^5$ km and $\log g = 4, 5$) and, since most exocomet detections have been made around A stars (e.g. the β Pic system, Zieba et al. 2019; Lecavelier des Etangs et al. 2022), a star with a photospheric temperature of 8200 K, $R_\star = 1.7R_\odot$ and $\log g = 4.0$. Although stellar luminosity is known to greatly influence the formation of cometary comae and tails (Lecavelier Des Etangs 1999), we used the same dust distributions for both stars.

The materials used for radiative transfer modeling are characterized by their composition and size distribution, as explained below. We utilize the *optool* package (Dominik et al. 2021) to obtain the complex dust particle opacities, using materials from *optool*’s material library, and assuming a specific grain size distribution. We consider different types of materials for our dust structures in the different simulations, but we assume that the whole simulation volume is homogeneous material-wise. Anisotropic scattering is treated by applying the Henyey-Greenstein function (option *scattering_mode_max* = 2 in RADMC-3D), and using the scattering opacity and g anisotropy parameters obtained for the specific material with *optool*. To be able to disentangle the effect of grain size, we use three size distributions. The number of particles (N) within these ranges is given by

$$N \propto a^{-q}. \quad (1)$$

We set the size distribution exponent $q = 3.5$ in all cases (Dohnanyi 1969). The size ranges of the three distributions are $a = 0.1\text{--}0.3 \mu\text{m}$ (labeled as 200 nm and corresponding to a mean size of 143.82 nm), $0.3\text{--}1.0 \mu\text{m}$ (650 nm, with a mean size of 439.51 nm) and $1.0\text{--}3.0 \mu\text{m}$ ($2 \mu\text{m}$), which corresponds to a mean particle size of 1438.2 nm. We selected these specific grain size intervals to sample the total scattering cross section provided by Pawellek et al. (2024), at the lower size ranges of that distribution, as well as the range where the rapid changes in the total cross section occur. Larger grains with a $\gtrsim 10 \mu\text{m}$ cause proportionally smaller extinction and increased brightness from forward scattering and are not considered in our present analysis. While in a real comet we likely see a mixture of different materials, our goal here is to see the effect of a single composition separately. Therefore, in our calculations, we use four different homogeneous compositions, in each case using each of the following material compositions separately: graphite (Draine 2003), amorphous pyroxene with 70% Mg content (Dorschner et al. 1995; Henning & Stognienko 1996), amorphous olivine with 50% Mg content (Dorschner et al. 1995; Henning & Stognienko 1996), and carbon grains (Zubko et al. 1996). While the choice of materials is arbitrary, we note that the carbonaceous (Woodward et al. 2021) and silicate dust (Wooden et al. 1999) is common in the comets of the Solar System. The debris disk of β Pictoris is also known

Passband	Solar-like star		A star	
	u_1	u_2	u_1	u_2
V (550 nm)	0.517	0.229	0.276	0.388
R (650 nm)	0.395	0.279	0.216	0.359
J (1200 nm)	0.149	0.334	0.064	0.300
H (1650 nm)	0.058	0.375	0.031	0.276
K (1650 nm)	0.041	0.327	0.015	0.236
L (3450 nm)	0.019	0.240	0.006	0.132

Table 1. Limb-darkening coefficients for the two stars considered in the light curve simulations, in the passbands where these calculations were carried out.

to host various silicates (Okamoto et al. 2004; Lu et al. 2022; Rebollido et al. 2024). In the case of a more realistic scenario when dust grains with different compositions are mixed, the total extinction / amount of scattered light can be obtained from the linear combination of the optical depths / scattered light contribution of the individual materials, assuming that the optical depth of the overall dust structure remains low ($\tau \ll 1$) and the radiation field is dominated by the radiation of the central star even inside the dust structure. As we will see, this is the case in our simulations. In case of Trans-Neptunian objects (in a frozen environment) the model spectra usually assume the presence of compound materials such as ices depleted to solid particles (e.g. Szabó et al. 2018). However, in case of comet Hale-Bopp, the spectra are well described as a sum of contributions of simple materials (pyroxene and olivine in particular Wooden et al. 1999). The lack of ice layer on comet dust in general seems to be plausible taken the low ice-to-dust ratio on comet layers into account, and the energetic irradiation field. For this reason, we restrict our simulations to homogeneous materials.

Extinction and forward-scattering light curves are calculated separately, assuming that the dust distribution (i.e. the comet) passes in the line of sight of the central star, orbiting it at a specific distance from the star (0.1 au on a circular orbit), the orbital plane is seen perfectly edge-on, and the occultation is central. We therefore neglect the impact of the orbital inclination (relative to the line of sight), which is known to influence the exact shape and depth of the transits (Lecavelier Des Etangs 1999).

For each light curve position, the central star is at a different location behind the density distribution (simulation volume). We cover the whole occultation event by changing the observer’s aspect angle by discrete intervals (0.1° during the transit itself, 0.2° – 0.05° out-of-transit). This is equivalent to the motion of the comet in front of the central star. The extinction light curve is obtained from the optical depth map, which is calculated by RADMC-3D for the specific observing geometry, convolved with the limb-darkened, resolved disk of the central star. We utilized the quadratic limb-darkening rule (Wade & Rucinski 1985), where the surface intensity of the star can be expressed as

$$\frac{I(\gamma)}{I(0)} = 1 - u_1 \cdot (1 - \cos(\gamma)) - u_2 \cdot (1 - \cos(\gamma))^2. \quad (2)$$

Here, γ is the angle between the normal vector on the stellar surface and the line of sight. We adopted the coefficients u_1 and u_2 from Claret (1998), these are listed in Table 1.

2.2. Light curve calculations

The forward-scattered light curve component corresponds to the total intensity of the surface brightness distribution of the same observing geometry, without the contribution of the central star (also directly obtained with RADMC-3D). It is calculated for a point source (assuming blackbody radiation), thus we neglect the effect of limb-darkening on this component. It can easily be scaled between the two stellar types (Solar-like and A-type star) by calculating the ratio of the emitted photons in each star. In this case, the A star we selected emits $4.1\times$ as many photons (at every wavelength), yielding $4.1\times$ higher amplitudes for this light curve component, as we show below. As a final step, we fit a spline function to interpolate both components of the light curves.

Extinction (defined as absorption plus scattering) efficiency of the dust grains depends on the size and material of a grain, as well as the phase angle. As the same amount (mass) of dust may consist of a larger number of smaller grains or smaller number of larger grains, in a random spatial distribution smaller grains cover a larger area, with an area increase proportional to the relative grain size, leading to an overall increased extinction cross section. However, this is complicated by the grain size dependence of the extinction efficiency that depends on the dielectric properties

of the grains. This is demonstrated in Fig. 2 (left panel) where we show the extinction coefficient for pyroxene grains, one of the materials used in our simulations, for different grain sizes.

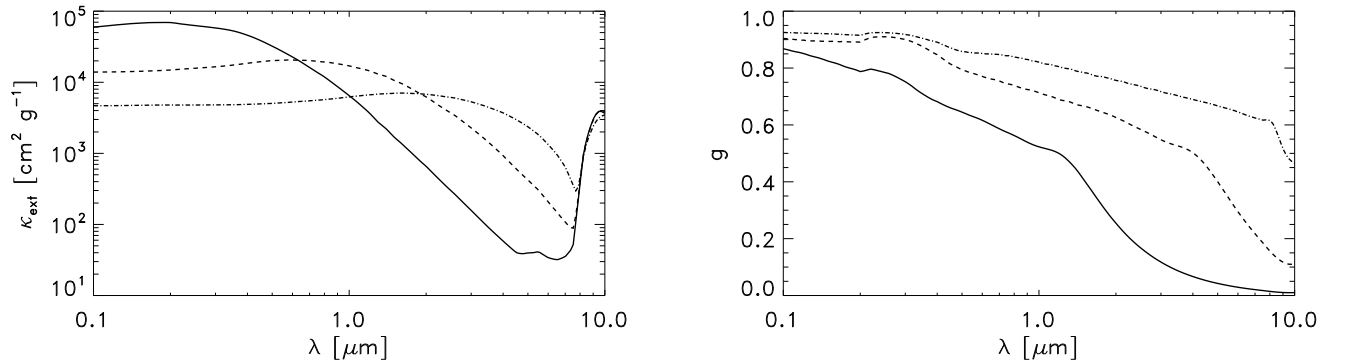


Figure 2. Left panel: Extinction coefficient as a function of wavelength for pyroxene grains with 70% Mg-content (Dorschner et al. 1995; Henning & Stognienko 1996). Right panel: g scattering parameter of the Henyey-Greenstein function as a function of wavelength, for different grain sizes, for the same material as in the left panel. The curves on both panels correspond to grain sizes of 200 nm (solid), 650 nm (dashed) and 2 μm (dash-dotted).

Scattering by dust grains is typically strongly phase angle dependent in the visible – near-infrared wavelength range (see e.g. Gordon 2004). The phase angle dependence in our simulations is characterized by the g scattering parameter of the Henyey-Greenstein scattering function – $g = 0$ corresponds to isotropic scattering, $g = -1$ dominant backward scattering, and $g = 1$ dominant forward scattering. An example is presented in Fig. 2 (right panel) for pyroxene grains, which show strong forward scattering for visible light, and moderate forward scattering for the near-infrared. Due to our modeling geometry – the dust structure is between us and the star, seen under a phase angle of $\phi \approx 180^\circ$ – our ‘observed’ light is dominated by forward scattered radiation. Thermal emission of the dust is also included in the radiative transfer calculations. The dust temperature is also dependent on the composition and grain size (see e.g. Henning & Stognienko 1996), and due to the proximity of the dust structure to the central star ($r_h = 0.1$ au) relatively high $T_d \approx 1000$ K dust temperatures are expected. However, as in our simulations the distance to the star remains constant during the transit and the optical depths are low ($\tau \ll 1$), the thermal emission contribution to the total brightness at a specific wavelength is constant before, during, and after the transit, meaning that it has no effect on the differential light curves.

The final “observable” light curve is the sum of the extinction and (forward-)scattering light curves. The calculated monochromatic light curves represent six common photometric bands: V (550 nm), R (650 nm), J (1.2 μm), H (1.65 μm), K (2.2 μm) and L (3.45 μm). We extrapolated the limb darkening coefficients for the L band (Table 1), which was not included in Claret (1998). These passbands were selected to represent the passband of PLATO (Rauer et al. 2014; Janssen et al. 2024) and to sample Ariel spectrographs (Tinetti et al. 2018, 2021; Szabó et al. 2022), while avoiding the computationally expensive approach of simulating entire wavelength ranges of specific instruments.

2.3. Density distributions

The input to our radiative transfer code is the spatial distribution of grains in the coma and possibly the tail in the comet. In the current stage, we can calculate the radiative transfer in a homogeneous environment built up by grains of a selected material with the same distribution of grain sizes everywhere in the coma.

First, our idea was to put actual images of selected Solar System comets directly in transit in front of an arbitrary star. However, this concept had incurable drawbacks and therefore had to be omitted. The most important issues were: i) The comets are seen in a 2D projection on the sky, while the radiative transfer has to be calculated in a 3D environment – including a third dimension in the distribution would have been mostly speculative rather than plausible; and ii) The scattering physics in a comet is complex. We see the actual comets because of the reflection properties of the dust at some specific illumination geometry, while we see the transiting exocomets because of the combination of absorption at a different, backlit geometry, together with components belonging to forward scattering.

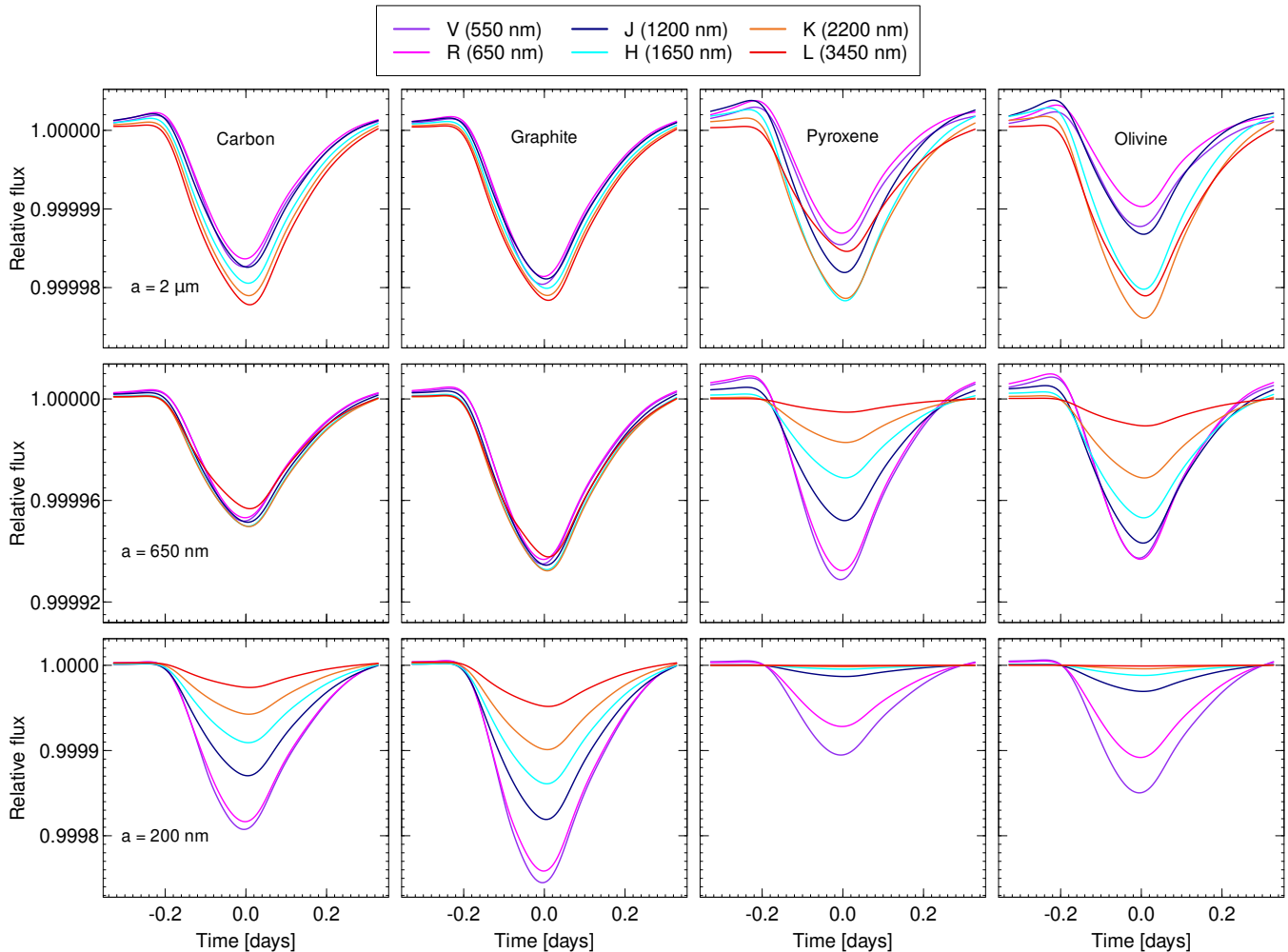


Figure 3. Synthetic, monochromatic light curves of a comet with narrow tail, plotted for the three selected grain size distributions, labelled as $a \sim 2 \mu\text{m}$ (top row), 650 nm (middle row) and 200 nm (bottom row), for an A star. Columns denote the materials used in the simulations: carbon (left), graphite (second from the left), pyroxene (second from the right), and olivine (right). Note the change in the scale of the y axis from row to row.

Without exact knowledge of material properties (spatially changing dust distributions, etc.) within the comet, the visible image cannot be plausibly converted into light scattering by that comet in transit.

Instead of using a combination of 2D images and additional more-or-less unfounded assumptions, we have chosen to base our model calculations entirely on mathematical foundations. This approach aligns well with the strength of our code, allowing us to calculate 3D distributions with homogeneous material properties. However, to ensure that our models are connected to the appearance of real comets, we used the visual appearance of observed Solar System comets as an inspirational source in the model design. We also aimed for a simple mathematical formalism and ultimately defined 3D distributions that accurately capture the impression of the chosen comets in their symmetry relationships and intensity distributions.

Our model parameters are therefore the material properties (which material, distribution of grain size) and the spatial density distribution. The actual cometary comae are known to follow a power-law light distribution that belongs to a spatial matter distribution of r^{-2} in the case of homogeneous and isotropic matter production (A'Hearn et al. 1984). This distribution has infinite extension and infinite mass – which does not occur in practice, of course, due to dust dynamics and dust fragmentation in a radiation environment. Describing this cutoff is difficult if not impossible analytically, and in the case of real comets, dust dynamics is calculated with numerical methods (Fulle 2004). In this paper, to avoid the issues of physical interpretation, we postulate that the truncating function is a

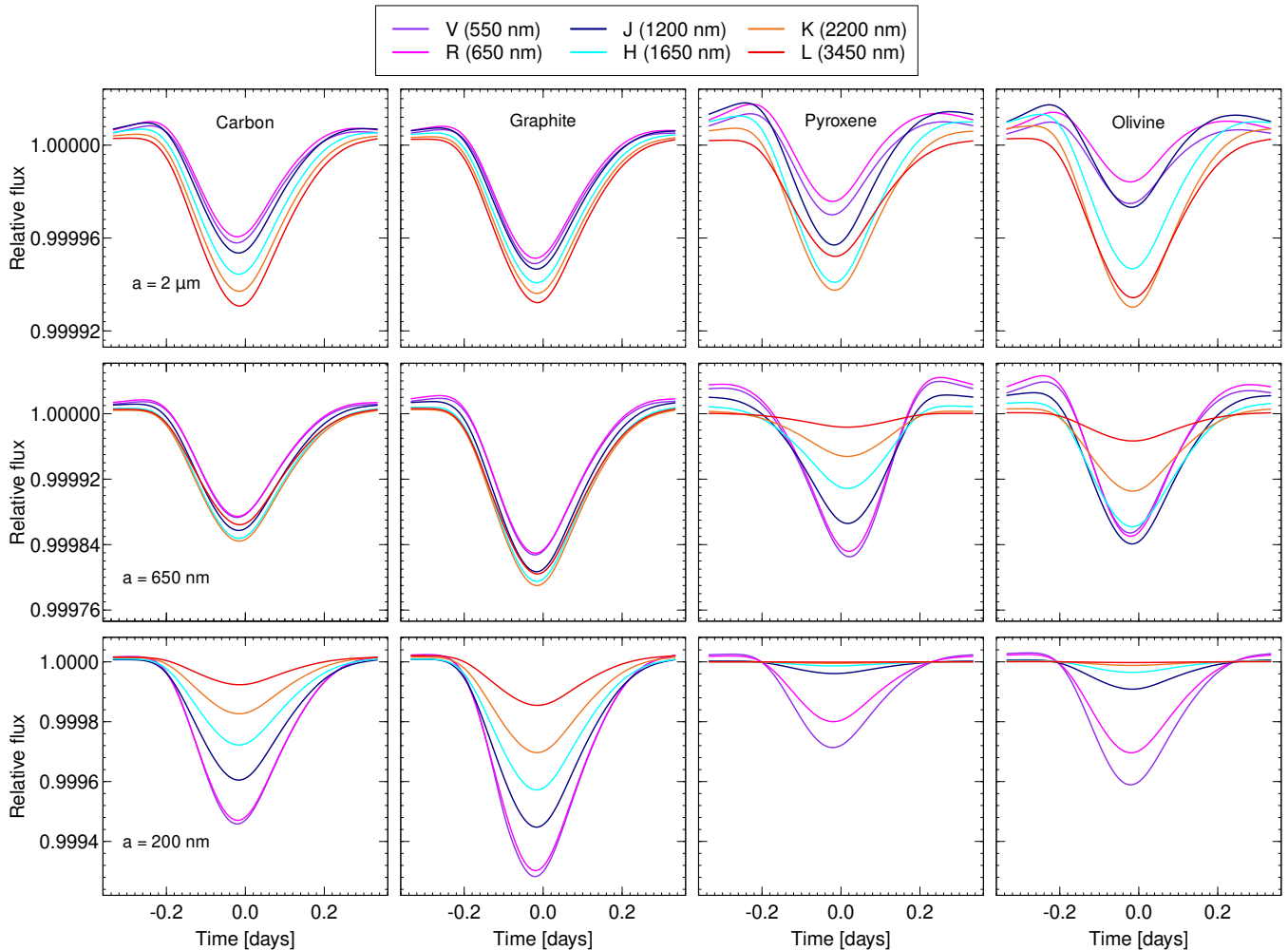


Figure 4. Same as Fig. 3 but for the comet model with a fan-like tail.

Gaussian distribution with finite extension. Although not fitting to any comet, this truncated model describes a light distribution that resembles most cometary comae.

For the demonstration presented in this paper, we selected three models with different weights and symmetry of the tail. Instead of the physical model of cometary activity presented in [Lecavelier Des Etangs et al. \(1999\)](#) which conveniently recreates the shape of a classical comet as explained by the so-called “fountain model” (e.g. [Alfven 1957](#); [Wallis 1968](#); [Wallis & MacPherson 1981](#)), we construct dust density distributions that resemble well-known comets from the Solar System. As a result, we can also study the way the shape of an exocomet might influence its transit light curve.

A comet with a narrow tail—We regard one of the fragments of Comet 73P/Schwassmann-Wachmann as the baseline for our simulations. In this case, the comet is assumed to have a central coma and a long tail (Fig. 1, left panels) to provide an appearance similar to that obtained by [Reach et al. \(2009\)](#). We assumed a three dimensional density distribution in the form of

$$\rho = \begin{cases} w_1 \rho_0 e^{-r^2/\sigma_1^2}/r^2 + (1 - w_1) \rho_0 e^{-(x^2+z^2)/\sigma_2^2} e^{-y^2/\sigma_f^2} & : y \geq 0 \\ w_1 \rho_0 e^{-r^2/\sigma_1^2}/r^2 + (1 - w_1) \rho_0 e^{-(x^2+z^2)/\sigma_2^2} e^{-|y|/\sigma_t} & : y < 0 \end{cases} \quad (3)$$

to represent such a comet, where $r^2 = x^2 + y^2 + z^2$. We set $w_1 = 0.2$, $\sigma_1 = 0.0015$ au, $\sigma_2 = 0.0025$ au, $\sigma_f = 0.0025$ au and $\sigma_t = 0.010$ au. This dust distribution also outlines the limitations of our modeling, and the deviation from

(Lecavelier Des Etangs et al. 1999; Lecavelier Des Etangs 1999; Zieba et al. 2019), since the tail of the cometary shape is truncated and we neglect the change in the distance between the star and each particle of the cometary tail.

A comet with a wide, fan-like tail—Here, a central dense coma is surrounded by a spherical structure that is extended in one direction (defined in the $+y$ direction in the simulation volume), but fades quickly in the opposite direction as in the case of Comet 29P/Schwassmann-Wachmann (Trigo-Rodríguez et al. 2008). In this case, we assumed the following density distribution:

$$\rho = \begin{cases} w_1\rho_0r^{-2}e^{-r^2/\sigma_1^2} + (1-w_1)\rho_0e^{-r^2/\sigma_2^2} & : y \geq 0 \\ w_1\rho_0r^{-2}e^{-r^2/\sigma_1^2} + (1-w_1)\rho_0e^{-(x^2+z^2)/\sigma_2^2}e^{-y^2/\sigma_t^2} & : y < 0 \end{cases} \quad (4)$$

The relative weights of the central and extended components are characterized by the weight factor w_1 , the core and extended structures are described by two Gaussians with width parameters σ_1 and σ_2 , and the fading tail is also described with a Gaussian with the width parameter σ_t in the $-y$ direction. We set $w_h = 0.5$, $\sigma_1 = 0.003$ au, $\sigma_2 = 0.012$ au and $\sigma_t = 0.006$ au in our calculations. The resultant distribution is shown in Fig. 1, in the middle panels.

A comet without tail—This density distribution is assumed to be fully spherically symmetric, that is, the density depends only on the radial distance r from the center of the comet. This density distribution was selected to resemble Comet 17P/Holmes during its 2007 outburst (e.g. Moreno et al. 2008a,b; Trigo-Rodríguez et al. 2008). The distribution is constructed as the sum of two 3D Gaussian profiles, characterized by the width parameters σ_1 and σ_2 . The relative weights of the two Gaussians are determined by the weight factor w_h . The central density ρ_0 is set for each simulation as described below. The spatial distribution of the density is determined as follows:

$$\rho = w_h\rho_0e^{-r^2/\sigma_1^2} + (1-w_h)\rho_0e^{-r^2/\sigma_2^2} \quad (5)$$

We applied $w_h = 0.7$, $\sigma_1 = 0.002$ au and $\sigma_2 = 0.008$ au.

To set up the dust distributions, our requirement was that the maximum optical depth (τ) in the simulation with the $a = 2 \mu\text{m}$ grain size is $\tau_R = 10^{-4}$ in the R band (650 nm) for the solar-like star, corresponding to the nominal maximum absorption depth² (AD) identified by Lecavelier des Etangs et al. (2022) in the β Pictoris system. This specifies a total dust mass that is then kept constant for the other grain sizes ($a = 200$ and 650 nm). These dust masses are listed in Table 2 below. In the following, we refer to the three dust distributions by the name of the comet that they are meant to resemble.

Comet name	carbon [10^{11} kg]	graphite [10^{11} kg]	pyroxene [10^{11} kg]	olivine [10^{11} kg]
No tail	2.96	4.14e+11	5.49e+11	6.98e+11
Fan-like tail	4.65	7.48	9.93	1.26
Narrow tail	0.84	1.35	1.80	2.29

Table 2. Total dust masses of the four materials used in the simulations, at the distance of $r_h = 0.1$ au.

3. RESULTS

Simulated light curves were calculated for each of the three model distributions in transit, assuming carbon, graphite, pyroxene, and olivine dust, and with a characteristic grain size in the coma/tail of 2 μm , 650 nm and 200 nm. Transit light curves were calculated in the 6 predefined wavelengths (resulting in 12 scenarios for comet each model, at every wavelength), yielding a 6-color photometric time series in each simulation. Template light curves are plotted in Figs. 3 – 5 for a star with spectral type A, and in 12–14 for a Solar-like star.

3.1. Light curve morphology

Figures 3 and 12 show the exocomet with a prominent thin tail, which is a morphologically somewhat similar distribution to what is expected from the fountain model (e.g. Alfvén 1957; Wallis 1968; Wallis & MacPherson 1981), leading

² We regard τ as the measure of the extinction component *only*, and AD as the measure of the combination of *both* light curve components (extinction and forward scattering). Thus, in a real observation scenario, only AD can be obtained.

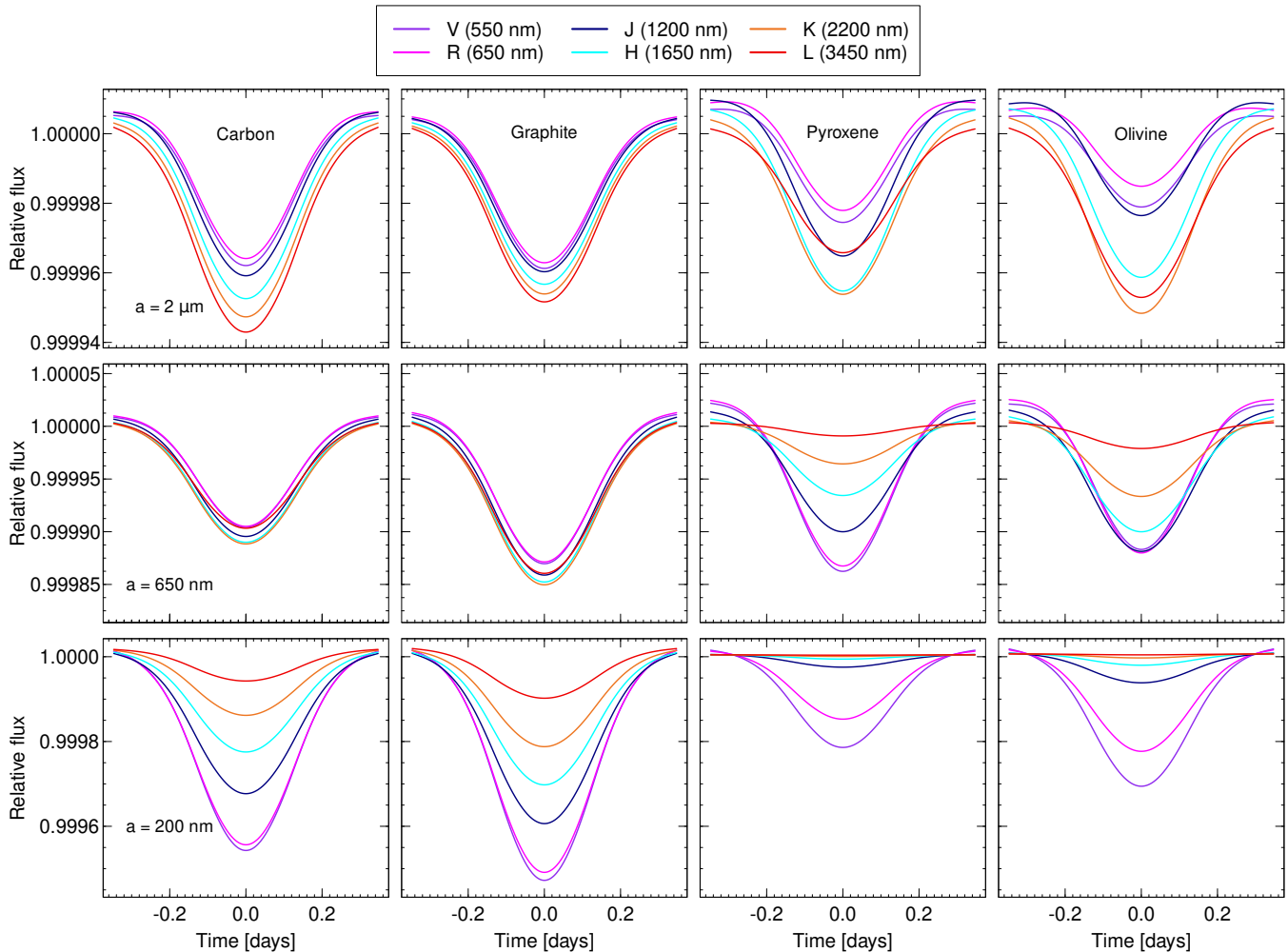


Figure 5. Same as Fig. 3 but for the comet model without a tail.

to sharkfin-like transit light curves. Indeed, on a qualitative comparison, the light curves in Figs. 3 and 12 closely resemble those seen in Lecavelier Des Etangs et al. (1999) and Lecavelier Des Etangs (1999). Our simulations also bear close resemblance to observed transit features that are attributed to exocometary activity, such as in Rappaport et al. (2018); Zieba et al. (2019); Lecavelier des Etangs et al. (2022), or a disintegrating exoplanet (Rappaport et al. 2012; Brogi et al. 2012). The light curves seen in Fig. 12 and especially in Fig. 3 readily reproduce the peak observable before the transit itself (Rappaport et al. 2018; Zieba et al. 2019), which is a consequence of the forward-scattered light.

Figs. 3 – 5 and 12–14 unanimously exhibit a common strong dependence of τ (and, as a consequence, AD) on the dust grain size, where smaller grain sizes generally yield deeper transits. This is especially true for carbon and graphite. This is a natural consequence of our calibration process, since all distributions of individual comets have the same total mass (Table 2). Figs. 6, 7, and 8 represent the measured AD for the three comet models considered. The well-known wavelength dependence of the scattering cross section (that is itself $\propto a^2$) means that while the light curves of a given material for a given a are topologically similar to each other, in the regime of small dust grains ($a \sim 200$ nm), the absorption depth varies considerably throughout the explored passbands. At the $2 \mu\text{m}$ dust size range, there are only comparatively minor differences in absorption depths at different wavelengths. Slightly larger differences in AD can be observed at the 650 nm grain sizes, where (unlike in 200 nm regime) AD increases towards the red end of the wavelength range (Figs. 6 – 8).

In all three cases, we see excess light before transit ingress. This is the contribution of forward scattering, the light coming from the dust grains, which are seen close to the edge of the star but are still not in transit. Because forward

scattering is efficient at very small deflection angles (Fig. 2), this contribution appears just before the transit (and is well known in the case of transits of evaporating/disintegrating planets as well (e.g. Rappaport et al. 2012; Garai 2018). The amplitude of the forward-scattered light also shows a clear dependence on both the material composition, the grain size, and the wavelength, dust distribution, and stellar spectral type (Fig. 9), with the highest amplitude (on the order of ≈ 90 ppm) occurring in the V and R bands, for olivine, in the case of the wide-tailed comet model. Fig. 9 also clearly shows that carbonaceous materials are less efficient at forward scattering, implying that the exocomet candidates observed by (Zieba et al. 2019) are not primarily made of these materials. Infrared wavelengths yield lower amplitudes for this component of the light curve. In this regime we observe a complete turnaround of the amplitudes as the $a = 200$ nm grain sized dust shows the highest amplitudes for the forward-scattered light, for the carbonaceous material.

The amplitude is also influenced by the shape of the comet itself, this manifests in the fact that the wide-tailed comet (Fig. 1) yields the highest amplitudes for this light curve component. Both comet models that own a tail component produce asymmetrical scattered light components, unlike the spherically symmetric coma alone.

A prominent difference between extinction and forward scattering is that the latter depends on the direct illumination of the dust. Therefore, the amplitude of the forward scattering components are scaled to arbitrary star-comet distances by $(r_h/1\text{au})^2$ as a first-order approximation (where r_h is the actual star-comet distance). In theory, the transit duration can be used to estimate r_h from a real exocomet transit observation (e.g. Boldog et al. 2023), which could then be used to put further investigate the cometary composition through the forward-scattered light. Because the extinction simply occurs due to blocking of a part of the line of sight, the extinction components (analogous to the transit depths) are independent of d (e.g. Mandel & Agol 2002), and depend only on the total scattering cross section of the dust. In this way, proper modeling of the forward scattering and the extinction together can also be used to reveal the star-to-transient distance via the ratio of the extinction to forward scattering.

Figs. 4–5 and 13–14 show transient light curves for comet models with increasing circular symmetry, that is, a fan-like tail and no tail at all. The combined light curve of the single coma (Figs. 5 and 14) also resembles a grazing transit of an exoplanet (e.g. Mancini et al. 2014). This is an important observation, because the shape of the transient itself is not a decisive diagnostics of the comet nature: exocomets (being similar to 17P/Holmes in outburst or other coma-dominated comets such as 1P/Encke for example) can also produce symmetrical light curve transients. On the other hand, possibly dust clumps (in a debris disk) unrelated to comets can also bear asymmetry that results in a more sharkfin-like transient feature. In these cases, we propose to observe the AD ratios (Figs. 6–8), or the “colors” directly during transit (16–19). The wide range in AD that is observed especially for the smallest grain sizes represented here (Figs. 6–8) implies that a spectrophotometric observation can be used to extract information regarding the material composition of an exocometary transit. This is discussed below.

The light curves are similar to each other between the two stars (a ‘solar-like’ and an A-type star) for all three given dust distributions. This is observed when comparing Figs. 3, 4, and 5 with 12, 13, and 14, respectively. One key difference is the Absorption Depth, as the same dust distribution transiting in front of the A spectral type star considered here (that is $1.7\times$ larger than the Sun-like star) yield transits that are $\leq 2\times$ shallower at each wavelength. In the cases of exoplanets, the planet is fully obscuring a portion of the stellar disk, leading to a direct way to estimate its size based on the transit depth (e.g. Seager & Mallén-Ornelas 2003), which is analogous to AD. For exocomets, no such straightforward method can exist to estimate the size based on the absorption depth, as it depends on a large number of factors, as shown above. We have also repeated the same calculations with a Solar-like host star, and we show the light curves in Appendix A.

3.2. Color index variations

When comparing Figures 3–5 and 12–14, the dependence of AD on the properties of the material and the characteristic size of the particles is evident. This is further emphasized by the direct comparison of AD (Figs. 6, 7, and 7), or the color variations (Figs. 16–19). The asymmetry of the dust distribution in combination with the (wavelength-dependent) limb darkening of the star yields ≈ 6 time brighter or fainter portions of the light curve (Figs. 16 and 15). This is a phenomenon previously known and extensively studied in the case of solar system comets (e.g. Jewitt & Meech 1986; Kolokolova et al. 1997; Luk’yanyk et al. 2019). However, the available time series data for extrasolar comets are currently monochromatic, so the value of AD ratios and colors has not been particularly emphasized until now.

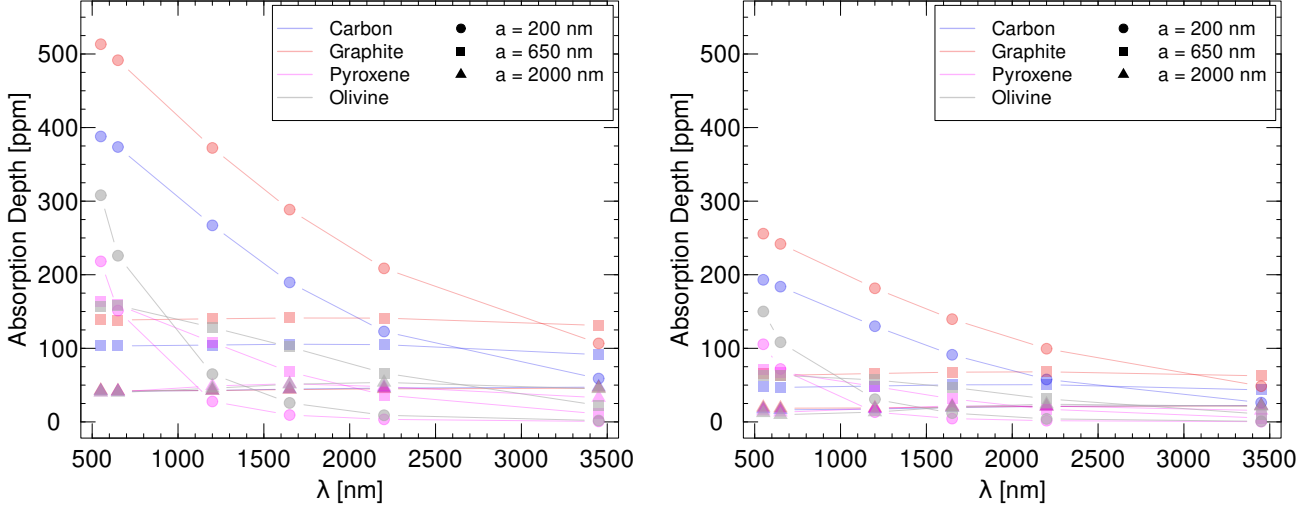


Figure 6. Absorption depth as a function of wavelength for the narrow-tailed comet (Fig. 1, left) for the Solar-like star (left) and the A star (right). The four materials considered (carbon, graphite, pyroxene, and olivine) are represented by colors (blue, red, magenta, and grey, respectively), while full circles, squares, and triangles correspond to the different dust grain sizes (200 nm, 650 nm, and $2\ \mu\text{m}$, respectively). Straight lines are shown for visualization purposes only.

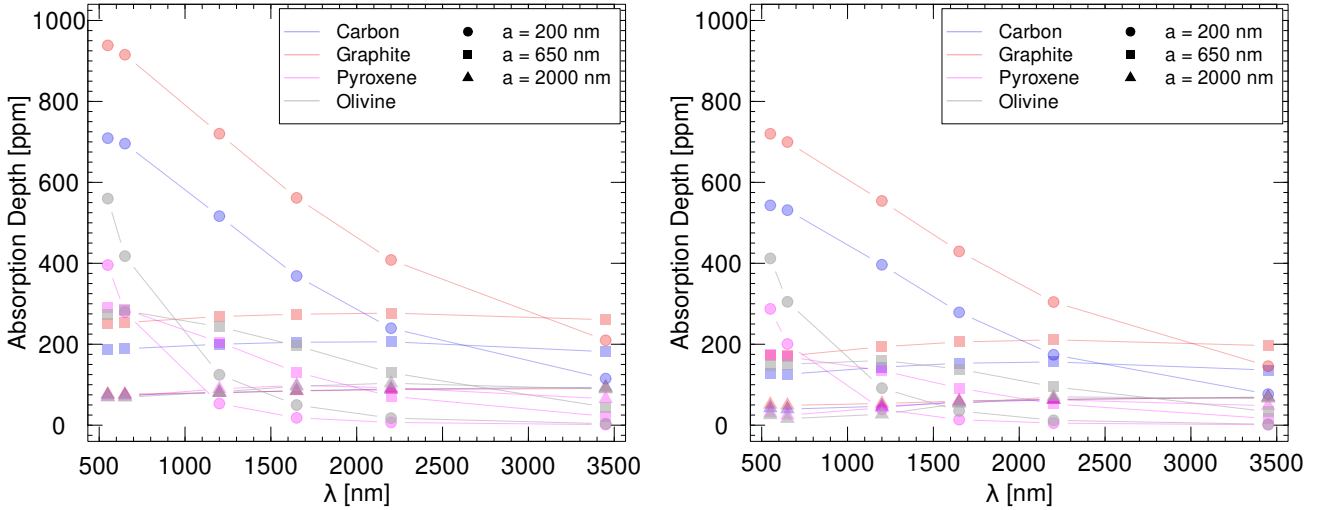


Figure 7. Absorption depth as a function of wavelength for the narrow-tailed comet (Fig. 1, left) for the Solar-like star (left) and the A star (right). The four materials considered (carbon, graphite, pyroxene, and olivine) are represented by colors (blue, red, magenta, and grey, respectively), while full circles, squares, and triangles correspond to the different dust grain sizes (200 nm, 650 nm, and $2\ \mu\text{m}$, respectively). Straight lines are shown for visualization purposes only.

We can observe that the smallest dust grains (~ 200 nm size range) produce transit light curves of significantly varying depth with the central wavelength. This is a “colorful” dust in transmission. In the case of carbonaceous dust (carbon and graphite) with 200 nm size, the optical V and R signals are the deepest, and they are very similar to each other, the V-R color index remains neutral during the transit, while the NIR components exhibit shallower transit light curves, which are material independent. We can observe the transit even in the L band as well, unlike in the case of silicates. When dust has a size range of $2\ \mu\text{m}$, the deepest signal is observed in the L band, the optical transit light curves are the most shallow ones, but with much less color difference than in the case of small dust. In between, at around 650 nm dust size ranges, the transit curves follow a very similar shape with close-to-neutral colors (i.e. near-constant AD, or color index of 1, Figs. 6–8, and 16 – 19). In summary, the same mass of carbonaceous

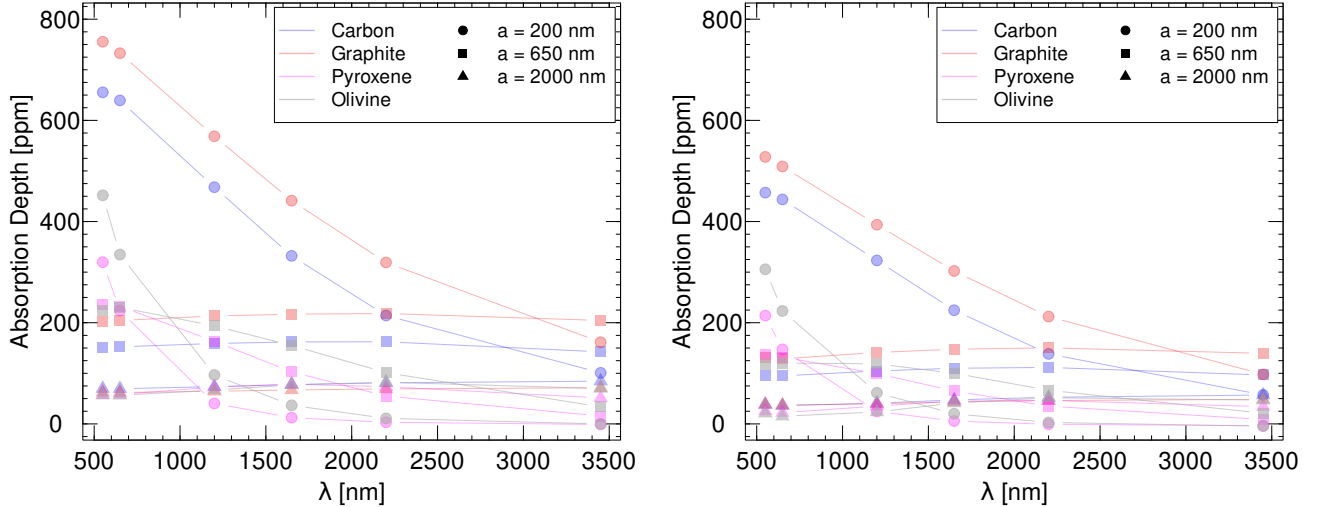


Figure 8. Absorption depth as a function of wavelength for comet without tail (Fig. 1, right) for the Solar-like star (left) and the A star (right). The four materials considered (carbon, graphite, pyroxene, and olivine) are represented by colors (blue, red, magenta, and grey, respectively), while full circles, squares, and triangles correspond to the different dust grain sizes (200 nm, 650 nm, and $2\ \mu\text{m}$, respectively). Straight lines are shown for visualization purposes only.

dust in transmission is “dark red”, “less dark neutral” and “pale blue” if the size range is ~ 200 , 650 and 2000 nm, respectively.

In the case of silicates, almost no variation is observed in the K and L bands in the case of the smallest dust distribution examined. The optical signal can be quite deep ($\sim 400\text{--}6000$ ppm in Figure 7, for 29P orbiting a solar-like star), but still less deep than in the case of carbonaceous materials. With increasing dust size, AD in the *NIR* bands also increases. In the case of the $2\ \mu\text{m}$ dust size, where the size of the scattering particles is compatible with the wavelength, the deepest signal will be observed in the H and K bands for pyroxene and olivine, respectively.

The change in color index becomes truly significant when the photometric transients are detected simultaneously in multiple bands. While differences can be seen by comparing the light curves, e.g. in Figs. 3–5, we quantitatively show the color variation curve in Appendix (B).

Exocomets are typically found in dusty environments, and transients related to the transit of overdensities in the hot dust cloud can lead to similar, nonperiodic transients. A substantial distinction between the two dust overdensity structures lies in the chemical differences and the different size distributions that can be discerned by multi-band observations. Dust clouds evolved in a warm environment and represent processed material, unlike exocomet dust, which originated freshly from a previously frozen environment and then underwent fragmentation, possibly presenting dust that has a different composition and grain size distribution than the warm dusty environment. Consequently, we anticipate that the transients of dusts will be only accompanied by minor changes in AD ratios at most, while exocomets will exhibit characteristic AD ratio changes that will also be consistent with our implemented code. This color information can distinguish between the two transient scenarios.

3.3. Transit timing variations

We also observe a change in the transit minima of the asymmetric dust distributions (Figs. 12, 3, 13, and 4) at different wavelengths. These are analogous to the transit timing variations (TTVs) of exoplanets (e.g. Agol et al. 2005). By extracting the times of minima (Figs. 10 and 11), we show that there may be significant offset at the different wavelengths. We note that $t = 0$ in our simulations corresponds to the collinearity of the observer, the center of dust distribution, and the center of the stellar disk. Due to the asymmetric dust distribution, the minimum of the light curve does not necessarily occur at $t = 0$. This phenomenon occurs because the limb-darkened stellar disk is convolved by the non-spherical comet tails of Figs. 1. We draw caution to the K- and L-band minima of the pyroxene-comets with $a = 200$ nm grain sizes, as these show extremely shallow transits, where the determination of the timings may be misleading, although these show the most significant discrepancy with the timing data at other wavelengths. We also

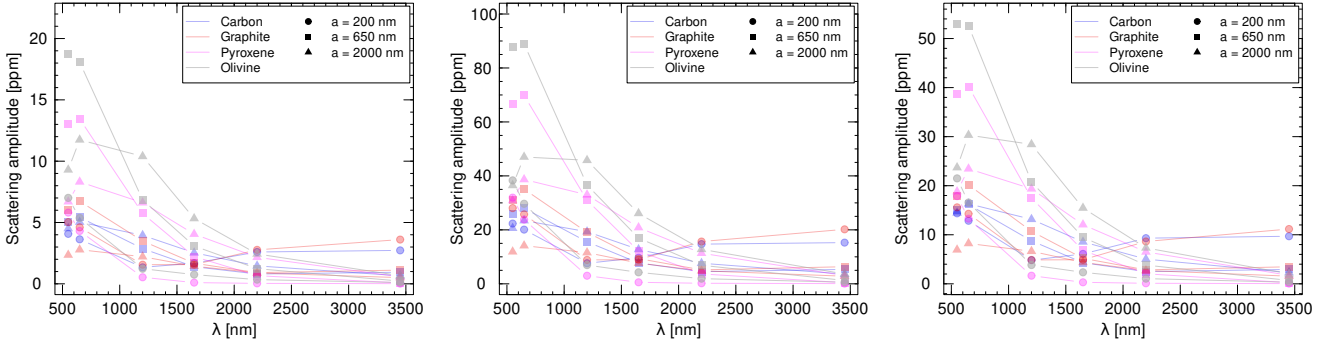


Figure 9. Amplitudes of the forward-scattered light for the three dust distributions shown on Fig. 1 (narrow-tailed comet – left, fan-like-tailed comet – middle, tailless comet – right) for the A star. Note the change in the scale of the y axis. Straight lines are shown for visualization purposes only.

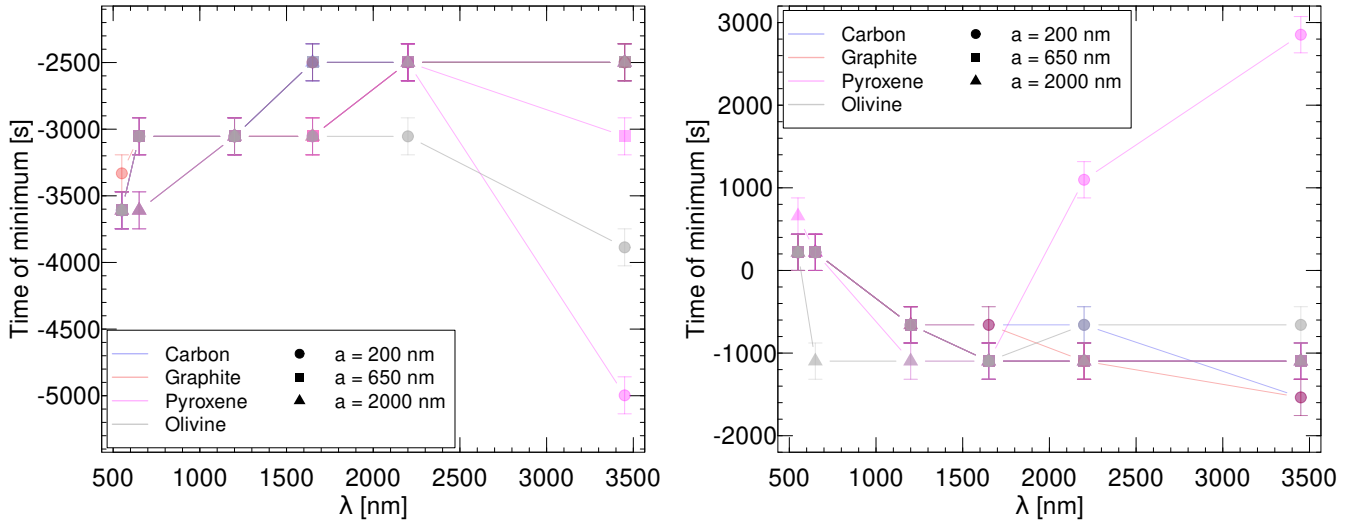


Figure 10. Extracted times of minima in the case of the narrow-tailed comet (Fig. 1, left) for the Sun-like star (left) and the A star (right). Straight lines are shown for visualization purposes only.

note that the transit timing data (Figs. 10 and 11) are estimated on the simulation grid (thus, only specific values can be recovered). The uncertainties are likewise estimated from the sampling on the grid.

3.4. Application to further surveys

The idea we present here is the multiband observation of nonperiodic photometric transients in stars with FEBs and/or dippers, and the evaluation of the observations in the light of AD ratios before, after and during the transients. There will likely be no unique solution for the multiband signals because the dust scattering scenario is complex and it has degenerations between the dust properties, the size distribution, and the total mass of dust in the line of sight. However, changing colors can still be observed and in favorable cases, the shift of the characteristic dust size can be proven. Here we review a few surveys where the multiband observations or multiband follow-ups promise a good possibility for an exocomet program.

TESS—Most of the known exocomet transits to date have been discovered by *TESS* (Ricker et al. 2015) in the β Pic system (Zieba et al. 2019; Lecavelier des Etangs et al. 2022). Given the apparent aperiodic or quasiperiodic nature of the transits themselves, continuous, survey-type photometry over long baselines appears to be the favored strategy. *TESS* has the advantage of long time series with almost continuous coverage. This is almost a compulsory requirement in “exocomet hunting”, because the transients occur unpredictably and have a duration in the order of 0.5-1 day – making them very hard to detect from the ground, most promisingly with an observatory network.

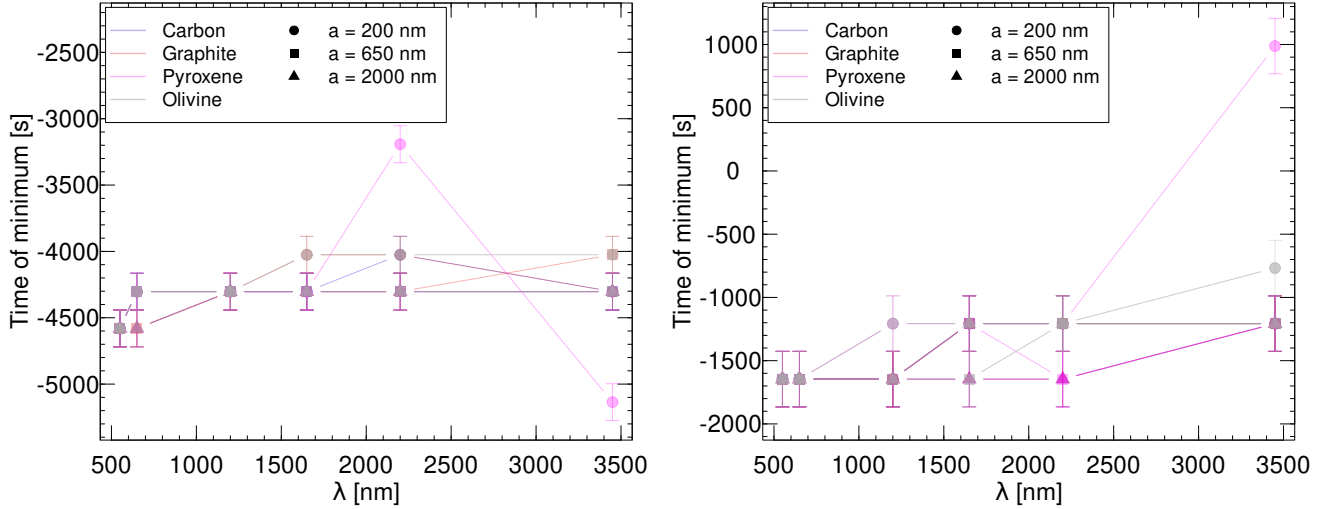


Figure 11. Extracted times of minima in the case of the wide-tailed comet (Fig. 1, middle) for the Sun-like star (left) and the A star (right). Straight lines are shown for visualization purposes only.

TESS represents the largest space photometry factory today, which makes it a prime instrument in exocomet search as well. However, TESS is a single-band photometer and, therefore, a targeted follow-up observation is required for multiband photometry purposes. These follow-up observations may have a longer cadence than the TESS data: space photometry shows the shape of the transient with good precision, while the follow-up observations have the task of measuring precise colors and confirm the presence of possible color variations, where the cadence can be longer than for the “transit shape” photometry.

CHEOPS—Well-tailored observations (with e.g. *CHEOPS*; Benz et al. 2021) of individual stellar systems can also yield interesting results. A transient feature, related to the debris disk surrounding DE Bootis, has been identified in its *CHEOPS* light curve by Boldog et al. (2023). A possible exocometary transit was identified in the HD 172555 system using its available *CHEOPS* observations (Kiefer et al. 2023). Here, synchronous follow-up observations with multiband instruments are also required to map the colors during the transients.

PLATO—With the 2026 launch of *PLATO* (Rauer et al. 2014), offering up to more than a year of uninterrupted ultra-high precision multicolor (Grenfell et al. 2020) light curves in the Long-duration Observation Phases (Nascimbeni et al. 2022), further detection of these transients is expected.

ARIEL—The upcoming *Ariel* mission (Tinetti et al. 2021) will be observing individual exoplanet systems from a target list. *Ariel* is planned to have the ability of synchronous visual + infrared photometry (VISPhot, FGS1 and FGS2; Szabó et al. 2022) together with NIR spectra taken by two low-resolution spectrographs (NIRSpec and AIRS Tinetti et al. 2021) with coverage up to $7.8 \mu\text{m}$, which is also capable of synthetic spectrophotometry. *Ariel* will be the first dedicated exoplanet space observatory with multiband abilities, and will be very much suited for a confirmation of the comet nature of dusty transients. Moreover, the low-resolution spectra from *Ariel* can indeed reveal the chemical constituents of the dusty transients, providing an important constraint to the deeper modeling and confirming the origin of them.

Rubin LSST—*LSST* will be a large wide-field ground-based survey designed to obtain repeated images that cover the entire southern celestial hemisphere and the Ecliptic. The 8.4 m telescope of the Rubin Vera Observatory will be equipped with a 3.2-gigapixel camera, and six filters (ugrizy) covering the wavelength range 320-1050 nm (Ivezić et al. 2019). *LSST* is not designed to collect photometric data series and, therefore, is not considered as an instrument to discover dippers or proven exocomet transits. Rather, it will be able to follow-up up the already known dippers of the southern sky, providing well calibrated 6 band photometry for 10 years of planned operation, with a pace of ~ 4 days. This can be combined with the uninterrupted space photometry of the dippers, revealing the transients with very good time resolution. The combined dataset will be very valuable to study practically any dipper in the southern sky together with the subtle changes of dust color over a very long time basis. This will be an unprecedented opportunity

to point out the changes of dust properties during the transient events which are compatible with exocomets, providing very strong evidence to this emerging scientific field.

4. SUMMARY AND CONCLUDING REMARKS

The conclusions of this article can be summarized in the following points.

- We have introduced an application based on RADMC-3D that allows simulating the transits of 3D, 256^3 pixelated comet models in front of stars at any photometric wavelength, assuming an arbitrary distance from the star, an arbitrary dust composition, and wavelength of observation.
- Inspired by the comets in the Solar System, we calculated transit models assuming compositions of carbonaceous (carbon and graphite) and silicate (pyroxene and olivine) dust, at the central wavelength of the VRJHKL band for three comet models with a thin tail, a fan-like tail, and no tail.
- The behavior of silicate and carbonaceous comet dust proved to be distinguishable in simulated VRJHKL transit observations. We also successfully simulated the dependence of wavelength-scattering cross-section curves on particle sizes.
- The origin of once-frozen comet dust in the dusty environment of extrasolar systems can be discerned from the hot/warm circumstellar dust mostly due to the differing size distribution, and the cometary nature can be confirmed through the different particle distributions and chemical compositions. Synchronous optical+NIR observations are well suited for this task.
- We presented some possible applications in planned space telescope missions in the present and near future.

Observational astrophysics of dippers and systems showing the FEB phenomenon and investigating possible exocomets in these systems are an emerging area in extrasolar astronomy. Our results demonstrated the potential of multiband observations in this field and point toward promising opportunities.

The project has been implemented with the support provided by the Ministry of Culture and Innovation of Hungary from the National Research, Development and Innovation Fund, financed under the SNN-147362 funding scheme. This work was partly supported by the K-138962 grant and the TKP2021-NKTA-64 excellence grant of the National Research, Development and Innovation Office (NKFIH, Hungary). SzK and GyMSz thank the support of the PRODEX Experiment Agreement No. 4000137122 between the ELTE Eötvös Loránd University and the European Space Agency (ESA-D/SCI-LE-2021-0025). This research has made use of the NASA Exoplanet Archive, which is operated by the California Institute of Technology, under contract with the National Aeronautics and Space Administration under the Exoplanet Exploration Program. Project no. C1746651 has been implemented with the support provided by the Ministry of Culture and Innovation of Hungary from the National Research, Development and Innovation Fund, financed under the NVKDP-2021 funding scheme. The generated light curves will be made publicly available upon acceptance of the paper at https://osf.io/ndjw6/?view_only=d9f0e84412a14e169e3de044628be6ab.

Facilities: Exoplanet Archive

Software: RADMC-3D (Dullemond et al. 2012), optool (Dominik et al. 2021)

REFERENCES

- Agol, E., Steffen, J., Sari, R., & Clarkson, W. 2005, MNRAS, 359, 567, doi: [10.1111/j.1365-2966.2005.08922.x](https://doi.org/10.1111/j.1365-2966.2005.08922.x)
- A’Hearn, M. F., Schleicher, D. G., Millis, R. L., Feldman, P. D., & Thompson, D. T. 1984, AJ, 89, 579, doi: [10.1086/113552](https://doi.org/10.1086/113552)
- Alfven, H. 1957, Tellus, 9, 92, doi: [10.3402/tellusa.v9i1.9064](https://doi.org/10.3402/tellusa.v9i1.9064)
- Altwegg, K., Balsiger, H., Bar-Nun, A., et al. 2015, Science, 347, 1261952, doi: [10.1126/science.1261952](https://doi.org/10.1126/science.1261952)
- Benz, W., Broeg, C., Fortier, A., et al. 2021, Experimental Astronomy, 51, 109, doi: [10.1007/s10686-020-09679-4](https://doi.org/10.1007/s10686-020-09679-4)
- Beust, H., & Morbidelli, A. 2000, Icarus, 143, 170, doi: [10.1006/icar.1999.6238](https://doi.org/10.1006/icar.1999.6238)

- Beust, H., & Valiron, P. 2007, *A&A*, 466, 201, doi: [10.1051/0004-6361:20053425](https://doi.org/10.1051/0004-6361:20053425)
- Beust, H., Vidal-Madjar, A., Ferlet, R., & Lagrange-Henri, A. M. 1994, *Ap&SS*, 212, 147, doi: [10.1007/BF00984518](https://doi.org/10.1007/BF00984518)
- Boldog, Á., Szabó, G. M., Kriskovics, L., et al. 2023, *A&A*, 671, A127, doi: [10.1051/0004-6361/202245101](https://doi.org/10.1051/0004-6361/202245101)
- Borucki, W. J., Koch, D., Basri, G., et al. 2010, *Science*, 327, 977, doi: [10.1126/science.1185402](https://doi.org/10.1126/science.1185402)
- Broggi, M., Keller, C. U., de Juan Ovelar, M., et al. 2012, *A&A*, 545, L5, doi: [10.1051/0004-6361/201219762](https://doi.org/10.1051/0004-6361/201219762)
- Claret, A. 1998, *A&A*, 335, 647
- d’Ischia, M., Manini, P., Martins, Z., et al. 2021, *Physics of Life Reviews*, 37, 65, doi: [10.1016/j.plrev.2021.03.002](https://doi.org/10.1016/j.plrev.2021.03.002)
- Dohnanyi, J. S. 1969, *J. Geophys. Res.*, 74, 2531, doi: [10.1029/JB074i010p02531](https://doi.org/10.1029/JB074i010p02531)
- Dominik, C., Min, M., & Tazaki, R. 2021, *OpTool: Command-line driven tool for creating complex dust opacities*, *Astrophysics Source Code Library*, record ascl:2104.010. <http://ascl.net/2104.010>
- Donn, B. 1963, *Icarus*, 2, 396, doi: [10.1016/0019-1035\(63\)90068-X](https://doi.org/10.1016/0019-1035(63)90068-X)
- Dorschner, J., Begemann, B., Henning, T., Jaeger, C., & Mutschke, H. 1995, *A&A*, 300, 503
- Draine, B. T. 2003, *ApJ*, 598, 1017, doi: [10.1086/379118](https://doi.org/10.1086/379118)
- Dullemond, C. P., Juhasz, A., Pohl, A., et al. 2012, *RADMC-3D: A multi-purpose radiative transfer tool*, *Astrophysics Source Code Library*, record ascl:1202.015. <http://ascl.net/1202.015>
- Encrenaz, T. 1984, *SSRv*, 38, 35, doi: [10.1007/BF00180336](https://doi.org/10.1007/BF00180336)
- Ferlet, R., Hobbs, L. M., & Vidal-Madjar, A. 1987, *A&A*, 185, 267
- Fray, N., Bardyn, A., Cottin, H., et al. 2016, *Nature*, 538, 72, doi: [10.1038/nature19320](https://doi.org/10.1038/nature19320)
- Fulle, M. 2004, in *Comets II*, ed. M. C. Festou, H. U. Keller, & H. A. Weaver, 565
- Gaidos, E. 2022, *Research Notes of the American Astronomical Society*, 6, 49, doi: [10.3847/2515-5172/ac5b7c](https://doi.org/10.3847/2515-5172/ac5b7c)
- Gaidos, E., Mann, A. W., Rojas-Ayala, B., et al. 2022, *MNRAS*, 514, 1386, doi: [10.1093/mnras/stac1433](https://doi.org/10.1093/mnras/stac1433)
- Garai, Z. 2018, *A&A*, 611, A63, doi: [10.1051/0004-6361/201629676](https://doi.org/10.1051/0004-6361/201629676)
- Gordon, K. D. 2004, in *Astronomical Society of the Pacific Conference Series*, Vol. 309, *Astrophysics of Dust*, ed. A. N. Witt, G. C. Clayton, & B. T. Draine, 77, doi: [10.48550/arXiv.astro-ph/0309709](https://doi.org/10.48550/arXiv.astro-ph/0309709)
- Grady, C. A., Brown, A., Welsh, B., et al. 2018, *AJ*, 155, 242, doi: [10.3847/1538-3881/aabe74](https://doi.org/10.3847/1538-3881/aabe74)
- Grady, C. A., Sitko, M. L., Bjorkman, K. S., et al. 1997, *ApJ*, 483, 449, doi: [10.1086/304230](https://doi.org/10.1086/304230)
- Graham, J. R., Kalas, P. G., & Matthews, B. C. 2007, *ApJ*, 654, 595, doi: [10.1086/509318](https://doi.org/10.1086/509318)
- Grenfell, J. L., Godolt, M., Cabrera, J., et al. 2020, *Experimental Astronomy*, 50, 1, doi: [10.1007/s10686-020-09660-1](https://doi.org/10.1007/s10686-020-09660-1)
- Henning, T., & Stognienko, R. 1996, *A&A*, 311, 291
- Ivezić, Ž., Kahn, S. M., Tyson, J. A., et al. 2019, *ApJ*, 873, 111, doi: [10.3847/1538-4357/ab042c](https://doi.org/10.3847/1538-4357/ab042c)
- Jannsen, N., De Ridder, J., Seynaeve, D., et al. 2024, *A&A*, 681, A18, doi: [10.1051/0004-6361/202346701](https://doi.org/10.1051/0004-6361/202346701)
- Jewitt, D., & Meech, K. J. 1986, *ApJ*, 310, 937, doi: [10.1086/164745](https://doi.org/10.1086/164745)
- Kennedy, G. M. 2018, *MNRAS*, 479, 1997, doi: [10.1093/mnras/sty1477](https://doi.org/10.1093/mnras/sty1477)
- Kennedy, G. M., Hope, G., Hodgkin, S. T., & Wyatt, M. C. 2019, *MNRAS*, 482, 5587, doi: [10.1093/mnras/sty3049](https://doi.org/10.1093/mnras/sty3049)
- Kiefer, F., Lecavelier des Etangs, A., Augereau, J. C., et al. 2014a, *A&A*, 561, L10, doi: [10.1051/0004-6361/201323128](https://doi.org/10.1051/0004-6361/201323128)
- Kiefer, F., Lecavelier des Etangs, A., Boissier, J., et al. 2014b, *Nature*, 514, 462, doi: [10.1038/nature13849](https://doi.org/10.1038/nature13849)
- Kiefer, F., Van Grootel, V., Lecavelier des Etangs, A., et al. 2023, *A&A*, 671, A25, doi: [10.1051/0004-6361/202245104](https://doi.org/10.1051/0004-6361/202245104)
- Kolokolova, L., Jockers, K., Chernova, G., & Kiselev, N. 1997, *Icarus*, 126, 351, doi: [10.1006/icar.1996.5660](https://doi.org/10.1006/icar.1996.5660)
- Kolokolova, L., Jockers, K., Gustafson, B. Å. S., & Lichtenberg, G. 2001, *J. Geophys. Res.*, 106, 10113, doi: [10.1029/2000JE001295](https://doi.org/10.1029/2000JE001295)
- Kral, Q., Wyatt, M. C., Triaud, A. H. M. J., et al. 2018, *MNRAS*, 479, 2649, doi: [10.1093/mnras/sty1677](https://doi.org/10.1093/mnras/sty1677)
- Kronk, G. W., Meyer, M., & Seargent, D. A. J. 2017, *Cometography: A Catalog of Comets, Volume 6, 1983-1993*, doi: [10.1017/9781139033947](https://doi.org/10.1017/9781139033947)
- Lagrange-Henri, A. M., Beust, H., Ferlet, R., & Vidal-Madjar, A. 1989, *A&A*, 215, L5
- Lecavelier Des Etangs, A. 1999, *A&AS*, 140, 15, doi: [10.1051/aas:1999114](https://doi.org/10.1051/aas:1999114)
- Lecavelier Des Etangs, A., Vidal-Madjar, A., & Ferlet, R. 1999, *A&A*, 343, 916, doi: [10.48550/arXiv.astro-ph/9812381](https://doi.org/10.48550/arXiv.astro-ph/9812381)
- Lecavelier des Etangs, A., Cros, L., Hébrard, G., et al. 2022, *Scientific Reports*, 12, 5855, doi: [10.1038/s41598-022-09021-2](https://doi.org/10.1038/s41598-022-09021-2)
- Levasseur-Regourd, A. C., Mukai, T., Lasue, J., & Okada, Y. 2007, *Planet. Space Sci.*, 55, 1010, doi: [10.1016/j.pss.2006.11.014](https://doi.org/10.1016/j.pss.2006.11.014)
- Lu, C. X., Chen, C. H., Sargent, B. A., et al. 2022, *ApJ*, 933, 54, doi: [10.3847/1538-4357/ac70d1](https://doi.org/10.3847/1538-4357/ac70d1)
- Luk’yanyk, I., Zubko, E., Husárik, M., et al. 2019, *MNRAS*, 485, 4013, doi: [10.1093/mnras/stz669](https://doi.org/10.1093/mnras/stz669)

- Mancini, L., Southworth, J., Ciceri, S., et al. 2014, *A&A*, 568, A127, doi: [10.1051/0004-6361/201424106](https://doi.org/10.1051/0004-6361/201424106)
- Mandel, K., & Agol, E. 2002, *ApJL*, 580, L171, doi: [10.1086/345520](https://doi.org/10.1086/345520)
- Marty, B. 2012, *Earth and Planetary Science Letters*, 313, 56, doi: [10.1016/j.epsl.2011.10.040](https://doi.org/10.1016/j.epsl.2011.10.040)
- Matrà, L., Dent, W. R. F., Wyatt, M. C., et al. 2017, *MNRAS*, 464, 1415, doi: [10.1093/mnras/stw2415](https://doi.org/10.1093/mnras/stw2415)
- Moreno, F., Ortiz, J. L., Santos-Sanz, P., et al. 2008a, *ApJL*, 677, L63, doi: [10.1086/587838](https://doi.org/10.1086/587838)
- . 2008b, *ApJL*, 684, L55, doi: [10.1086/592043](https://doi.org/10.1086/592043)
- Nascimbeni, V., Piotto, G., Börner, A., et al. 2022, *A&A*, 658, A31, doi: [10.1051/0004-6361/202142256](https://doi.org/10.1051/0004-6361/202142256)
- Okamoto, Y. K., Kataza, H., Honda, M., et al. 2004, *Nature*, 431, 660, doi: [10.1038/nature02948](https://doi.org/10.1038/nature02948)
- Pavlenko, Y., Shubina, O., Kulyk, I., et al. 2021, *Kinematics and Physics of Celestial Bodies*, 37, 64, doi: [10.3103/S0884591321020057](https://doi.org/10.3103/S0884591321020057)
- Pawellek, N., Moór, A., Kirchschrager, F., et al. 2024, *MNRAS*, 527, 3559, doi: [10.1093/mnras/stad3455](https://doi.org/10.1093/mnras/stad3455)
- Poch, O., Istiqomah, I., Quirico, E., et al. 2020, *Science*, 367, aaw7462, doi: [10.1126/science.aaw7462](https://doi.org/10.1126/science.aaw7462)
- Rappaport, S., Levine, A., Chiang, E., et al. 2012, *ApJ*, 752, 1, doi: [10.1088/0004-637X/752/1/1](https://doi.org/10.1088/0004-637X/752/1/1)
- Rappaport, S., Vanderburg, A., Jacobs, T., et al. 2018, *MNRAS*, 474, 1453, doi: [10.1093/mnras/stx2735](https://doi.org/10.1093/mnras/stx2735)
- Rauer, H., Catala, C., Aerts, C., et al. 2014, *Experimental Astronomy*, 38, 249, doi: [10.1007/s10686-014-9383-4](https://doi.org/10.1007/s10686-014-9383-4)
- Reach, W. T., Vaubillon, J., Kelley, M. S., Lisse, C. M., & Sykes, M. V. 2009, *Icarus*, 203, 571, doi: [10.1016/j.icarus.2009.05.027](https://doi.org/10.1016/j.icarus.2009.05.027)
- Rebollido, I., Eiroa, C., Montesinos, B., et al. 2020, *A&A*, 639, A11, doi: [10.1051/0004-6361/201936071](https://doi.org/10.1051/0004-6361/201936071)
- Rebollido, I., Stark, C. C., Kammerer, J., et al. 2024, *AJ*, 167, 69, doi: [10.3847/1538-3881/ad1759](https://doi.org/10.3847/1538-3881/ad1759)
- Redfield, S. 2007, *ApJL*, 656, L97, doi: [10.1086/512237](https://doi.org/10.1086/512237)
- Ricker, G. R., Winn, J. N., Vanderspek, R., et al. 2015, *Journal of Astronomical Telescopes, Instruments, and Systems*, 1, 014003, doi: [10.1117/1.JATIS.1.1.014003](https://doi.org/10.1117/1.JATIS.1.1.014003)
- Roberge, A. 2014, *Nature*, 514, 440, doi: [10.1038/514440a](https://doi.org/10.1038/514440a)
- Seager, S., & Mallén-Ornelas, G. 2003, *ApJ*, 585, 1038, doi: [10.1086/346105](https://doi.org/10.1086/346105)
- Strøm, P. A., Bodewits, D., Knight, M. M., et al. 2020, *PASP*, 132, 101001, doi: [10.1088/1538-3873/aba6a0](https://doi.org/10.1088/1538-3873/aba6a0)
- Szabó, G. M., Kiss, C., Pinilla-Alonso, N., et al. 2018, *AJ*, 155, 170, doi: [10.3847/1538-3881/aab14e](https://doi.org/10.3847/1538-3881/aab14e)
- Szabó, G. M., Kálmán, S., Pribulla, T., et al. 2022, *Experimental Astronomy*, 53, 607, doi: [10.1007/s10686-021-09777-x](https://doi.org/10.1007/s10686-021-09777-x)
- Tajiri, T., Kawahara, H., Aizawa, M., et al. 2020, *ApJS*, 251, 18, doi: [10.3847/1538-4365/abb17](https://doi.org/10.3847/1538-4365/abb17)
- Tinetti, G., Drossart, P., Eccleston, P., et al. 2018, *Experimental Astronomy*, 46, 135, doi: [10.1007/s10686-018-9598-x](https://doi.org/10.1007/s10686-018-9598-x)
- Tinetti, G., Eccleston, P., Haswell, C., et al. 2021, *arXiv e-prints*, arXiv:2104.04824, doi: [10.48550/arXiv.2104.04824](https://doi.org/10.48550/arXiv.2104.04824)
- Tobin, W., Barnes, S. I., Persson, S., & Pollard, K. R. 2019, *MNRAS*, 489, 574, doi: [10.1093/mnras/stz1983](https://doi.org/10.1093/mnras/stz1983)
- Trigo-Rodríguez, J. M., Davidsson, B., Montanes-Rodríguez, P., Sanchez, A., & Troughton, B. 2008, in *39th Annual Lunar and Planetary Science Conference, Lunar and Planetary Science Conference*, 1627
- Trigo-Rodríguez, J. M., García-Melendo, E., Davidsson, B. J. R., et al. 2008, *A&A*, 485, 599, doi: [10.1051/0004-6361:20078666](https://doi.org/10.1051/0004-6361:20078666)
- Vidmachtenko, A., & Steklov, A. 2013, *Astronomical School's Report*, 9, 146
- Wade, R. A., & Rucinski, S. M. 1985, *A&AS*, 60, 471
- Wallis, M. K. 1968, *Planet. Space Sci.*, 16, 1221, doi: [10.1016/0032-0633\(68\)90028-7](https://doi.org/10.1016/0032-0633(68)90028-7)
- Wallis, M. K., & MacPherson, A. K. 1981, *A&A*, 98, 45
- Welsh, B. Y. 2019, *Mem. Soc. Astron. Italiana*, 90, 581
- Welsh, B. Y., & Montgomery, S. L. 2018, *MNRAS*, 474, 1515, doi: [10.1093/mnras/stx2800](https://doi.org/10.1093/mnras/stx2800)
- Wooden, D. H., Harker, D. E., Woodward, C. E., et al. 1999, *ApJ*, 517, 1034, doi: [10.1086/307206](https://doi.org/10.1086/307206)
- Woodward, C. E., Wooden, D. H., Harker, D. E., et al. 2021, *PSJ*, 2, 25, doi: [10.3847/PSJ/abca3e](https://doi.org/10.3847/PSJ/abca3e)
- Zieba, S., Zwintz, K., Kenworthy, M. A., & Kennedy, G. M. 2019, *A&A*, 625, L13, doi: [10.1051/0004-6361/201935552](https://doi.org/10.1051/0004-6361/201935552)
- Zubko, V. G., Mennella, V., Colangeli, L., & Bussoletti, E. 1996, *MNRAS*, 282, 1321, doi: [10.1093/mnras/282.4.1321](https://doi.org/10.1093/mnras/282.4.1321)

APPENDIX

A. LIGHT CURVES FOR A SUN-LIKE STAR

In this section, we show the light curves calculated in Sections 3 (Figs. 3–5), but for a Solar-like host star (Figs. 12–14). The light curves are morphologically similar, whereas quantitative deviations occur due to the differing stellar radius and the differing limb darkening (see its discussion in 2.2).

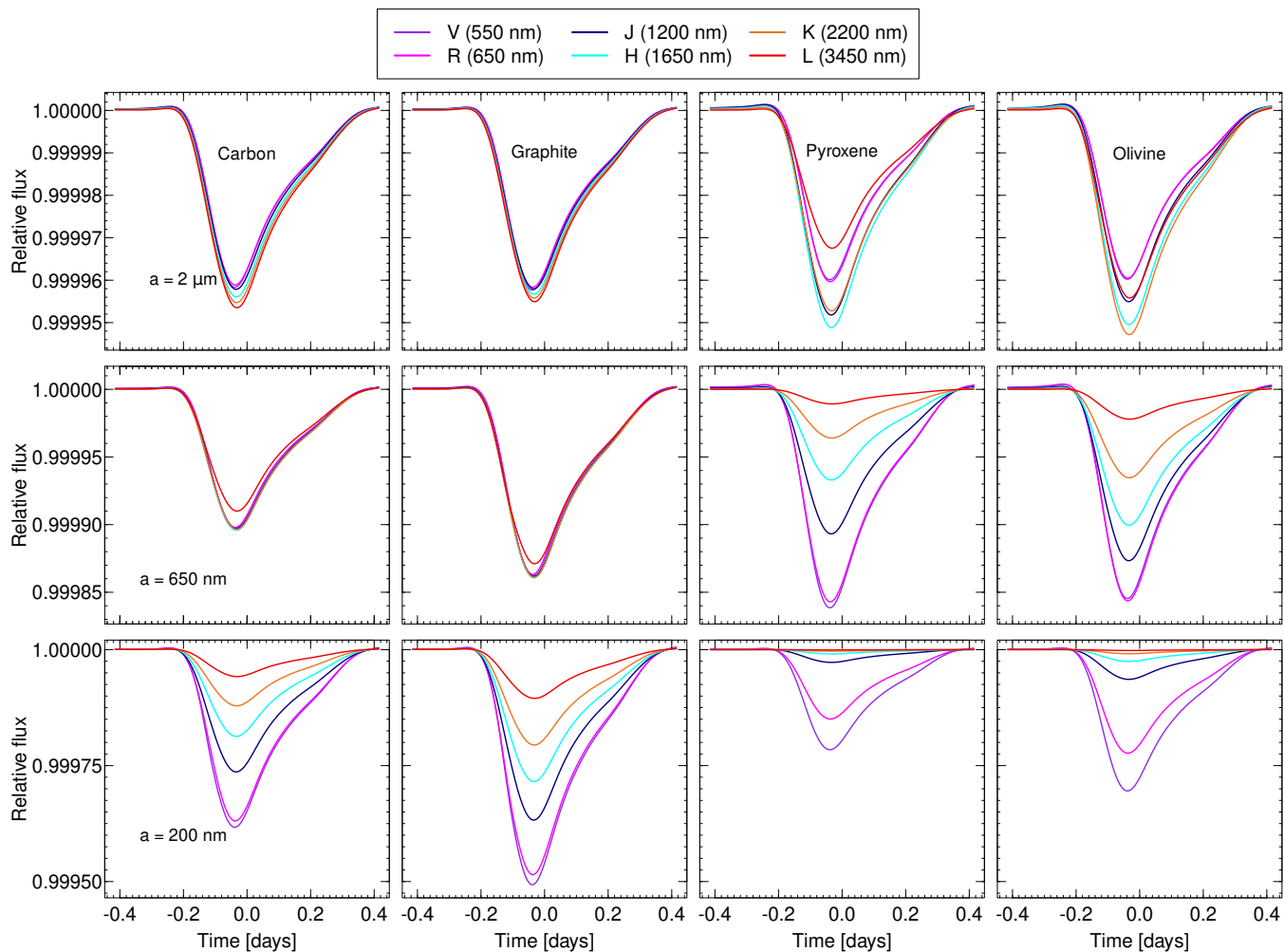


Figure 12. Same as Fig. 3 but the transits are calculated for solar-like star.

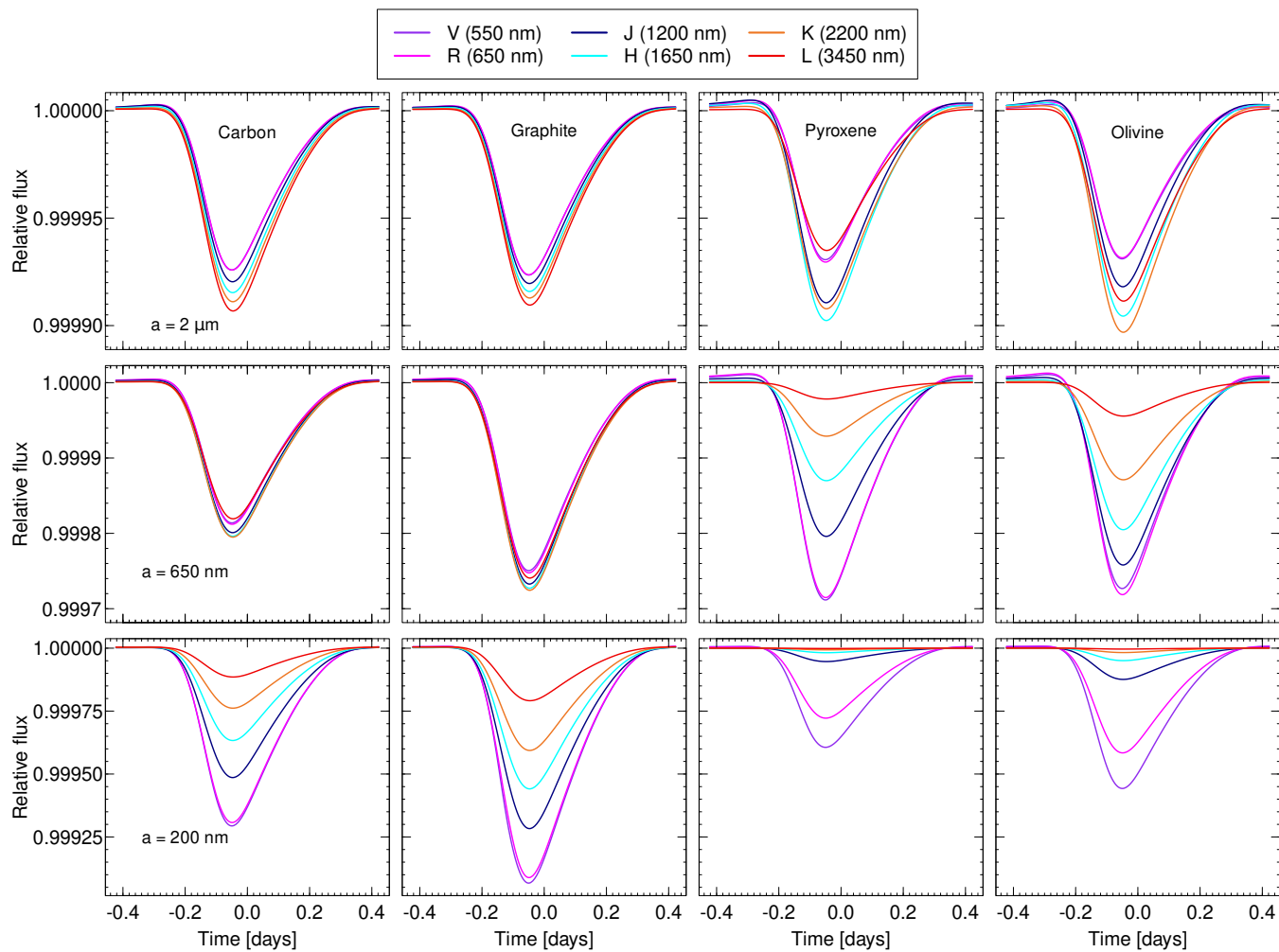


Figure 13. Same as Fig. 4 but the transits are calculated for Solar-like star.

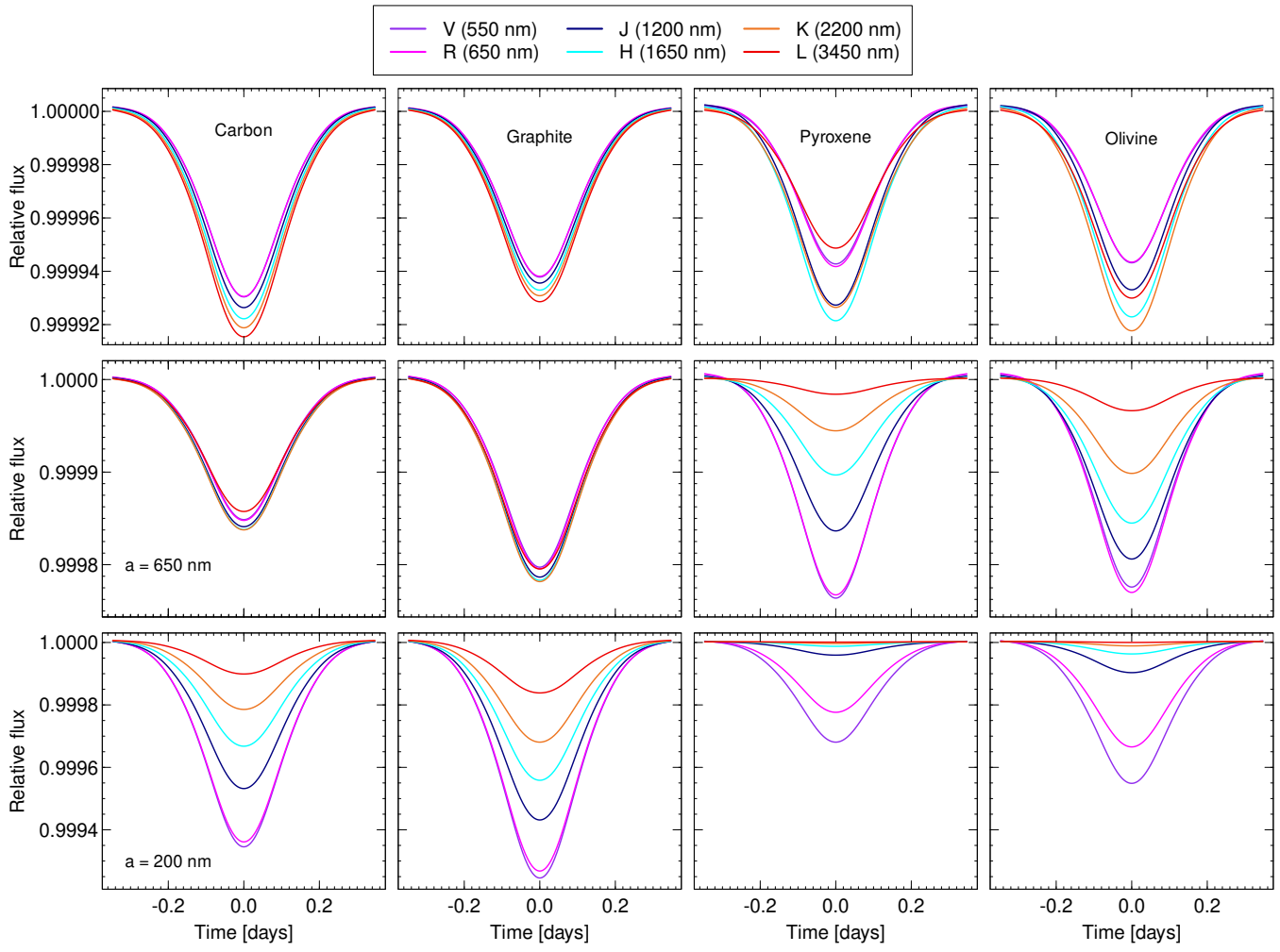


Figure 14. Same as Fig. 5 but the transits are calculated for a Solar-like star.

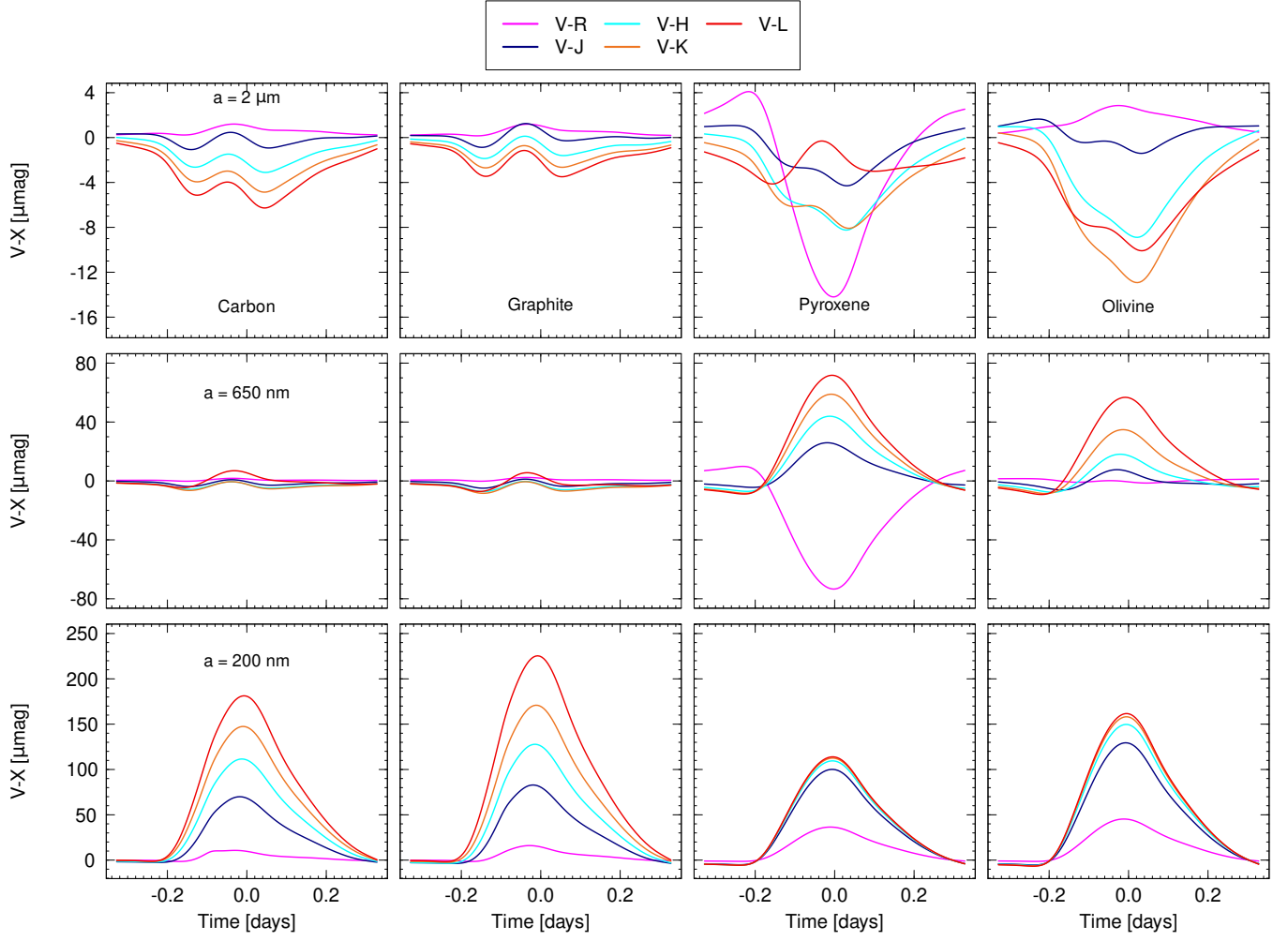


Figure 15. Color variations for the narrow-tailed comet (Fig. 1) orbiting an A star.

B. COLOR VARIATIONS

In this section, we plot the differential light curves calculated in different simulation bandpasses. These figures show the color of the total stellar light after having traveled through the comet dust and suffered a spatially dependent transfer, including both outward and inward scattering. The figures are plotted in units of μmag , and the $V - X$ colors indicate a redder color towards positive values (see its discussion in Sect. 2.2).

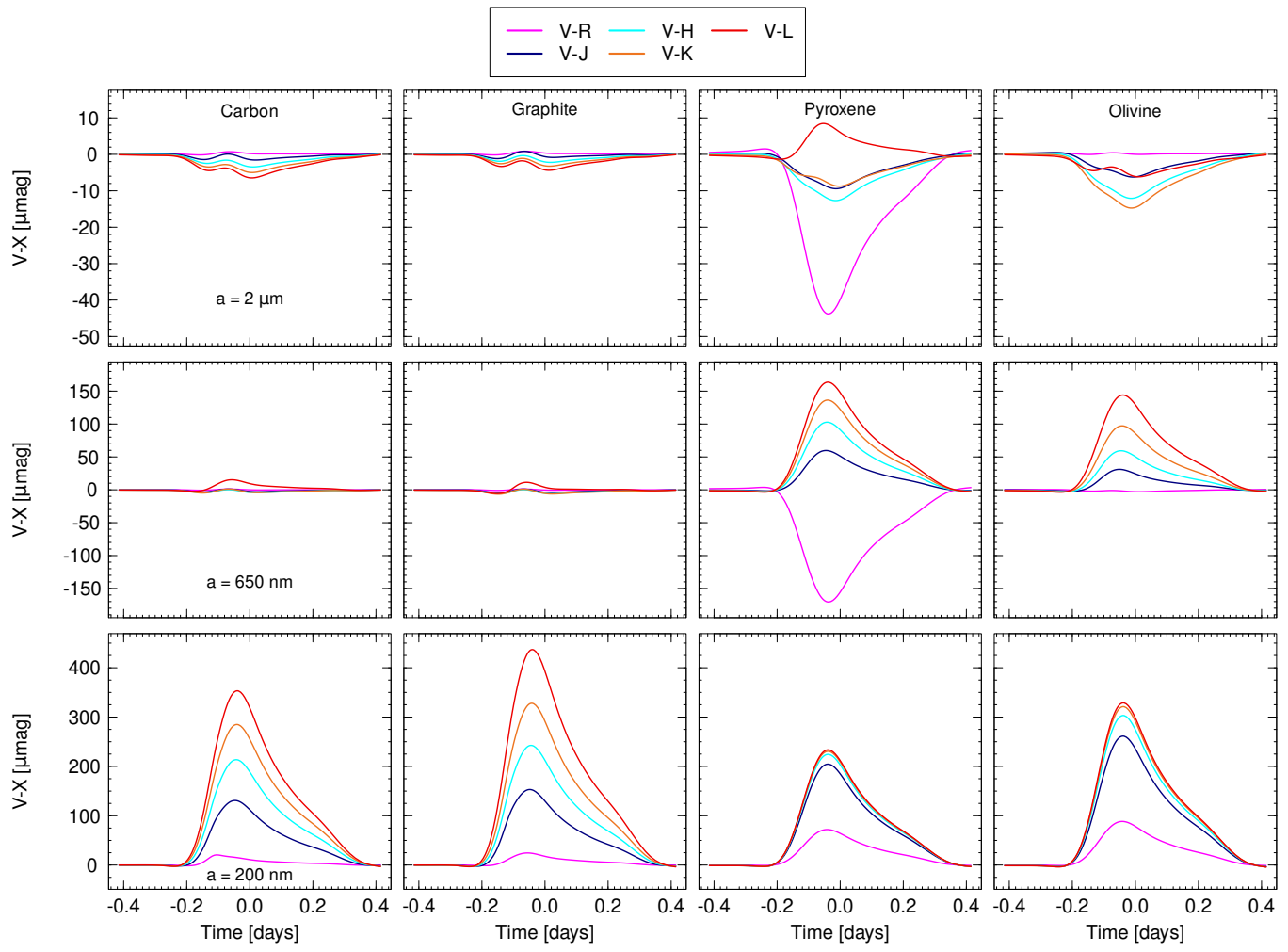


Figure 16. Color variations for the narrow-tailed comet (Fig. 1) orbiting a solar-like star.

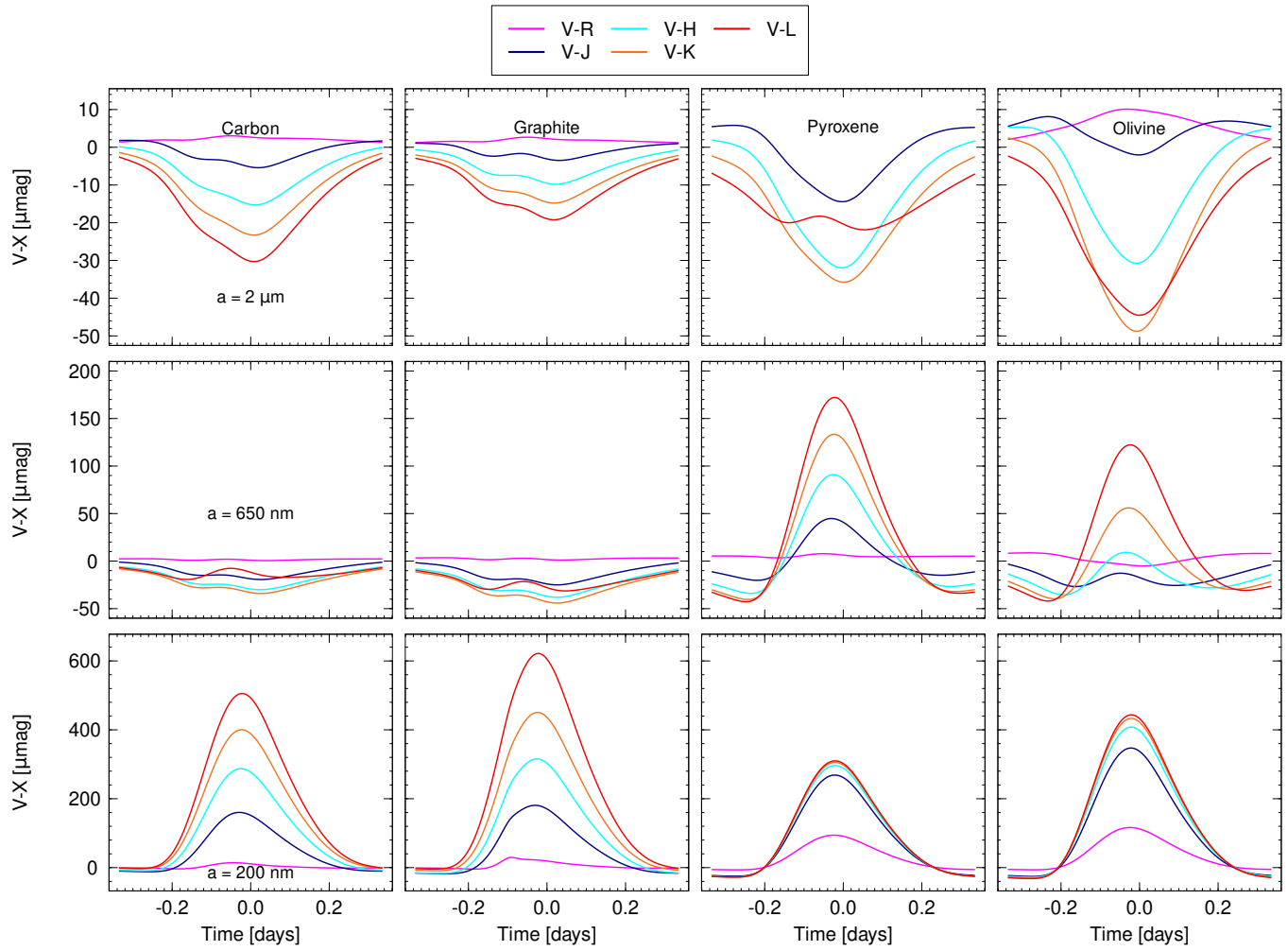


Figure 17. Color variations for the wide-tailed comet (Fig. 1) orbiting an A star.

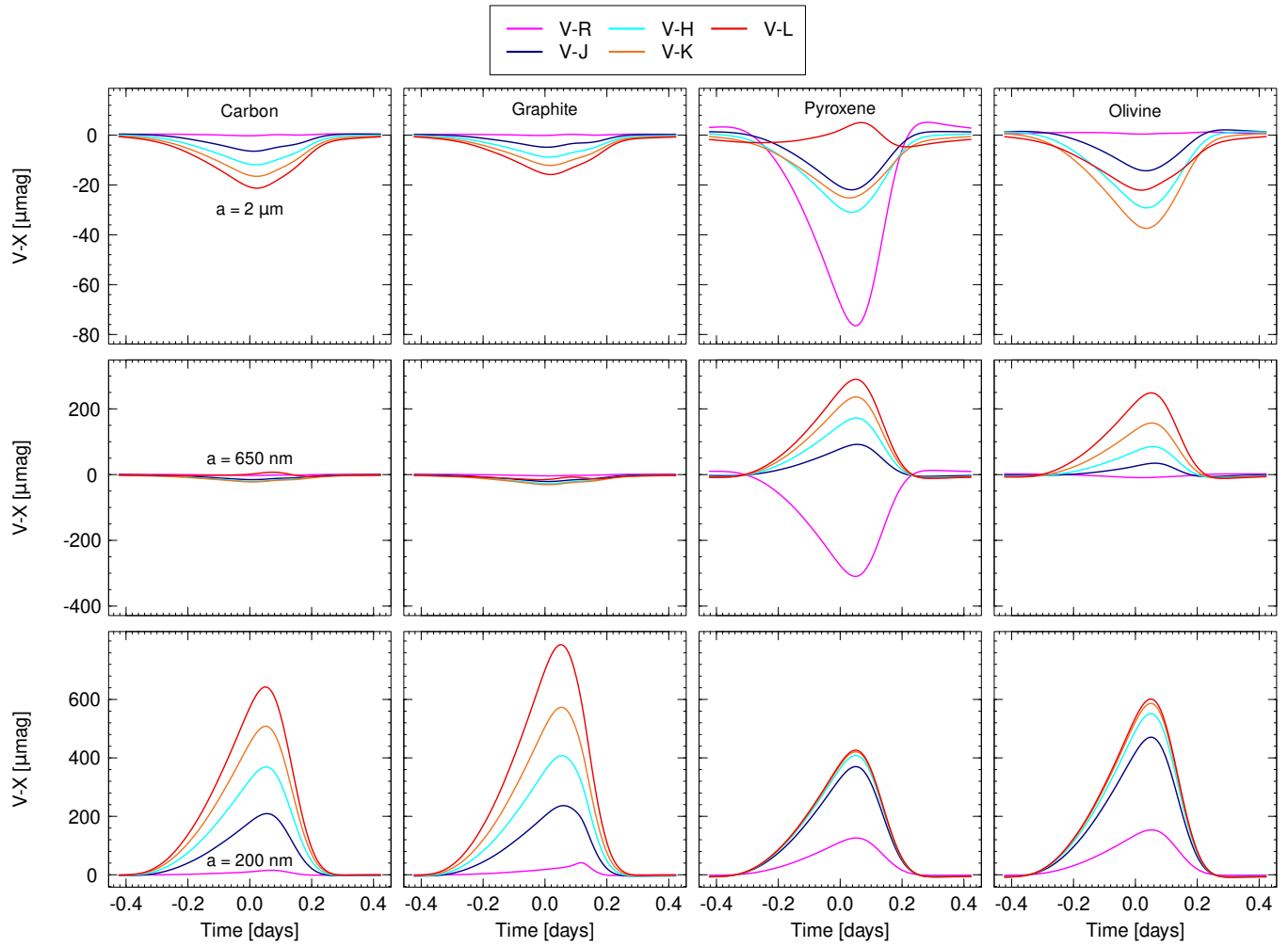


Figure 18. Color variations for the wide-tailed comet (Fig. 1) orbiting a solar-like star.

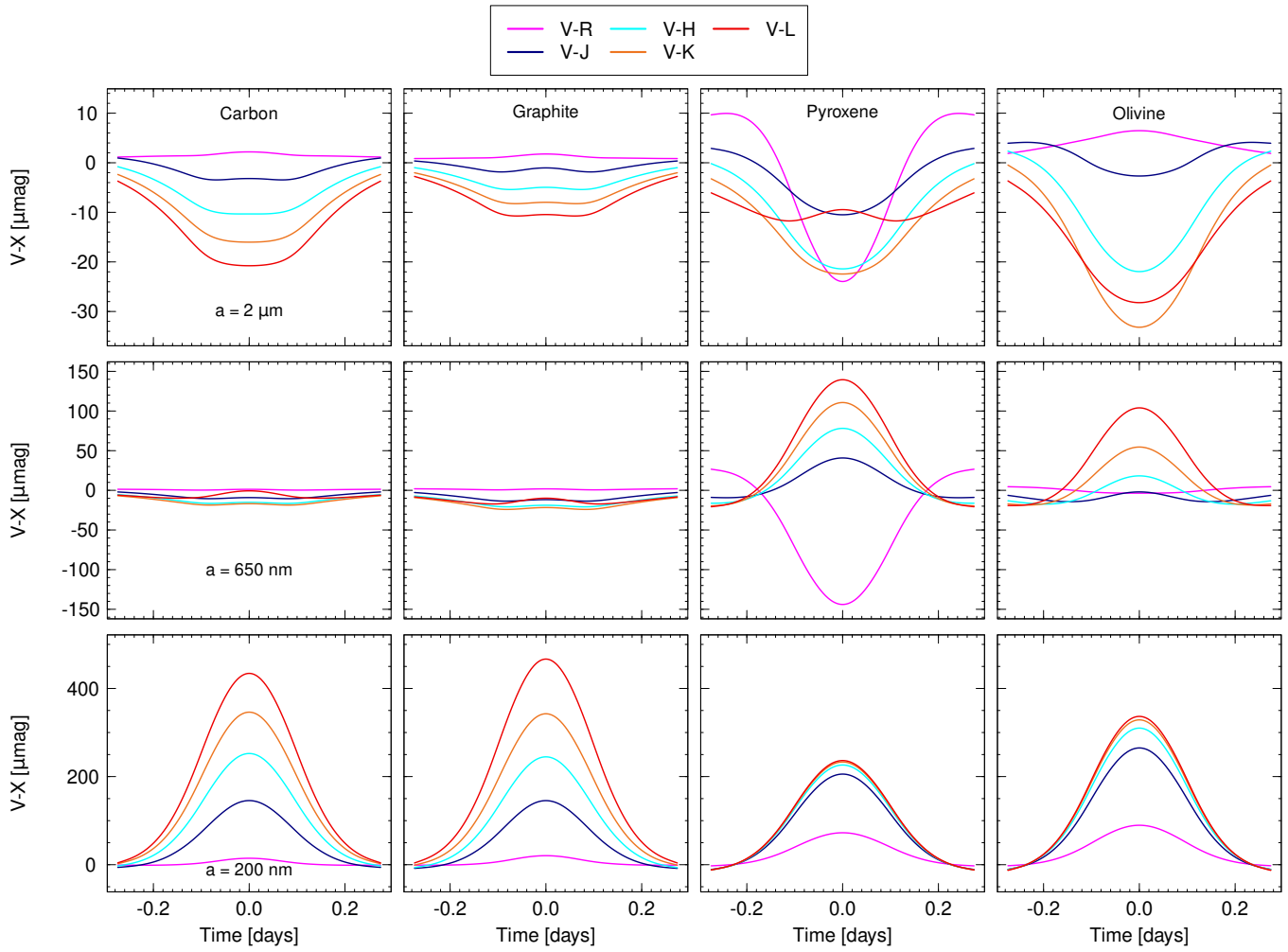


Figure 19. Color variations for spherically symmetric comet (1) orbiting an A star.

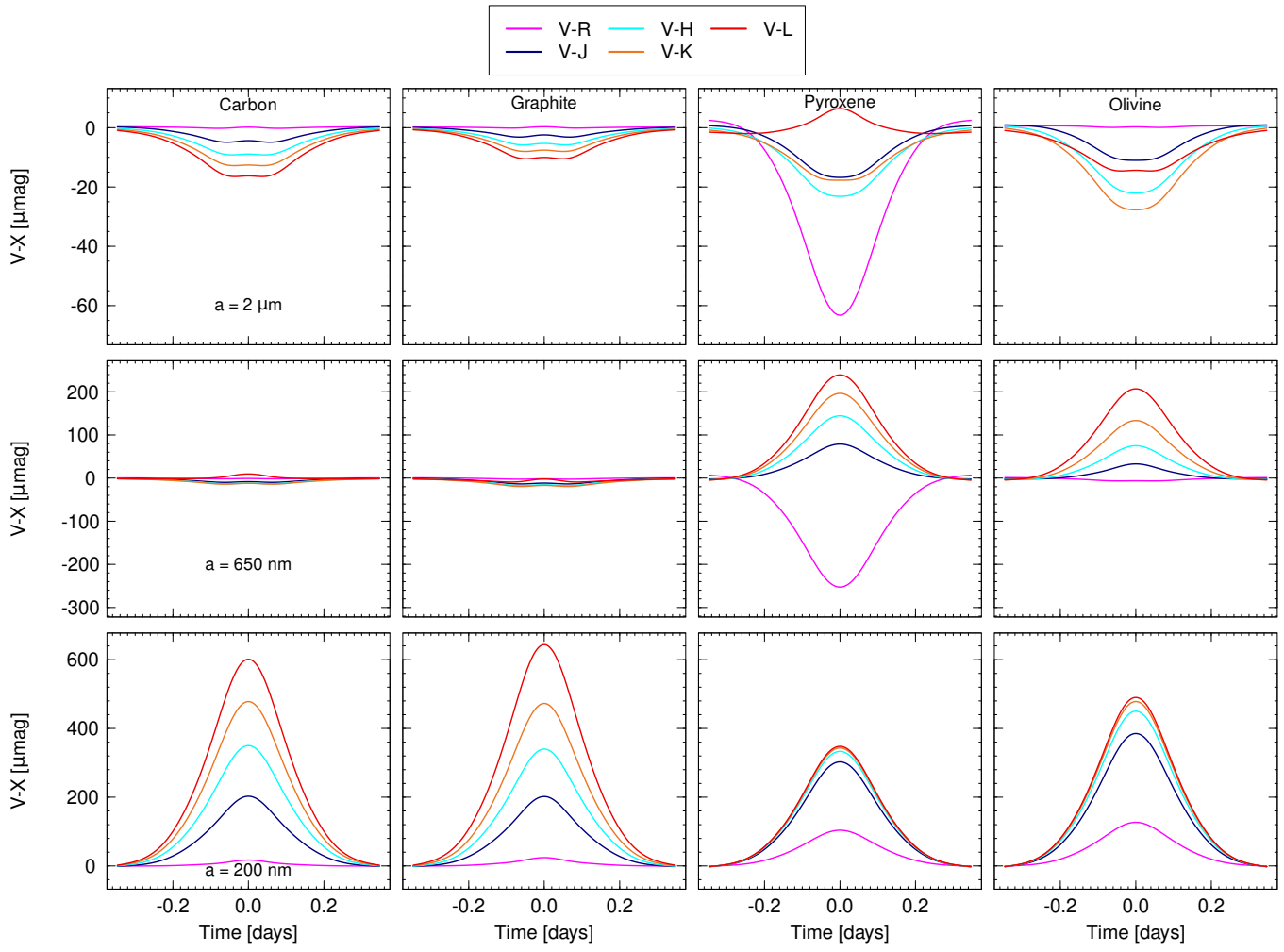


Figure 20. Color variations for spherically symmetric comet (Fig. 1) orbiting a solar-like star.